# Antigen presentation by tumor-associated macrophages mediates progenitor to terminal exhaustion transition in GBM and other solid tumors

## AUTHORS

Jessica Waibl Polania[1], Alexandra Hoyt-Miggelbrink[1], William H. Tomaszewski[2], Lucas P. Wachsmuth[1,3], Selena J. Lorrey[2], Daniel S. Wilkinson[4], Emily Lerner[3,5], Karolina Woroniecka[1], John B. Finlay[3], and Peter E. Fecci[4,6,*]

## AFFILIATIONS

[1]Department of Pathology, Duke University School of Medicine, Durham, NC 27710, USA

[2]Department of Immunology, Duke University, Durham, NC 27710, USA

[3]Duke Medical Scientist Training Program, Duke University School of Medicine, Durham, NC 27710, USA

[4]Department of Neurosurgery, Duke University School of Medicine, Durham, NC 27710, USA

[5]Department of Biomedical Engineering, Duke University, Durham, NC 27710, USA

[6]Lead contact

*Correspondence: peter.fecci@duke.edu

# GRAPHICAL ABSTRACT

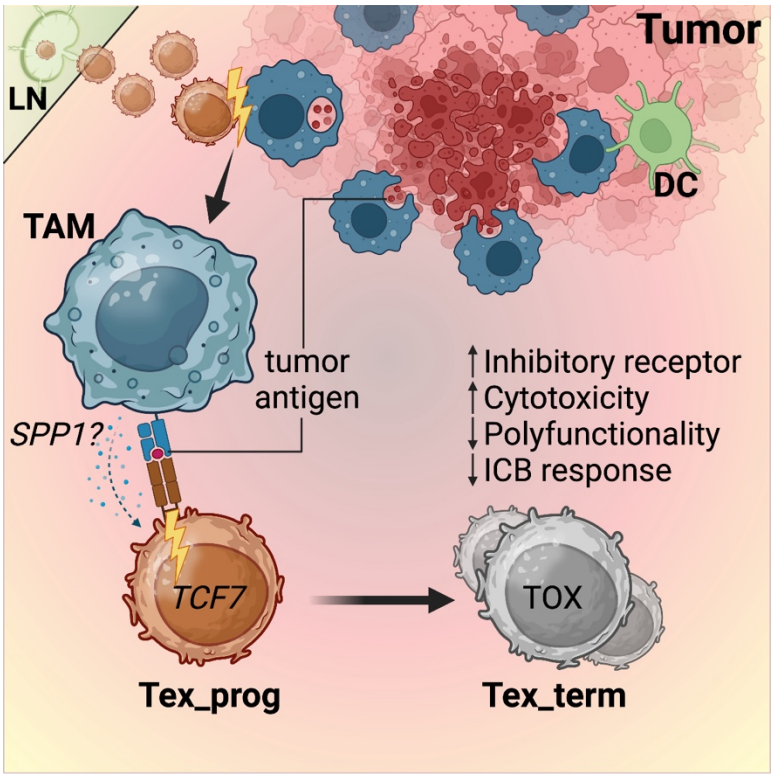

# SUMMARY

While terminally exhausted T cells (Tex_term) retain important anti-tumor cytotoxic function, it is the relative preservation of renewable, stem-like progenitor exhaustion (Tex_prog) that better indicates immunotherapeutic responsivity. Although restraining the progression from Tex_prog to Tex_term thus takes on clinical significance, the cellular interactions in a tumor microenvironment (TME) governing such progression remain less established. Employing glioblastoma (GBM) and other solid tumors as models of severe exhaustion, we provide a detailed characterization of the progression from Tex_prog to Tex_term within the TME, where we observe a striking and disproportionate loss of Tex_prog over time, leading to a low progenitor exhaustion to terminal exhaustion ratio (PETER). We find exhaustion concentrated within tumor-specific T cell subsets, with cognate antigenic exposure requisite for acquisition of the Tex_term phenotype. However, we implicate tumor-associated macrophages (TAM), and not tumor cells, as the source of antigenic exposure governing the Tex_prog to Tex_term transition. Using cell – cell interaction analysis, we additionally highlight candidate receptor–ligand communications that may be specifically mediating the progression to Tex_term and resultant decline in PETER within the TME.



# KEYWORDS

T cell exhaustion, tumor-associated macrophage, tumor microenvironment, tumor immunology, immunotherapy, brain tumor, brain metastasis, glioblastoma


# INTRODUCTION

Brain tumors, both primary and metastatic, continue to herald poor survival[1,2]. Immunotherapies, such as immune checkpoint blockade (ICB) and chimeric antigen receptor (CAR) T cells, continue to hold promise for improving outcomes, but remain only marginally effective within the intracranial confines[3,4]. This has been especially true in the case of primary malignant brain tumors, such as glioblastoma (GBM)[5]. An established

contributor to immunotherapeutic failures in GBM is tumor-imposed T cell dysfunction, particularly exhaustion[6-13]. T cell exhaustion is a differentiation state characterized by progressive and hierarchical loss of effector functions following chronic antigen exposure[14-17]. As we have previously shown, it is particularly severe in GBM,[18] making GBM an important model tumor for studying the dynamics and contributors to T cell exhaustion. Two subsets of T cell exhaustion have now been described by several groups: progenitor exhaustion (Tex_prog) and terminal exhaustion (Tex_term)[19-21]. Tex_prog describes a stem-like state, characterized by the expression of PD1 and TCF1 (surrogate Ly108), which retains T cell polyfunctionality and is immunotherapy-responsive[21]. Tex_prog may subsequently differentiate toward Tex_term, which, in turn, is characterized by high expression of TOX, PD1 and TIM3. Terminally exhausted T cells have greater cytotoxic capability, but are short-lived and non-replenishing[15,16,21]. Various studies have suggested that promoting the maintenance of Tex_prog is an important consideration for generating an immunotherapy-responsive tumor microenvironment (TME)[19-22]. Details of the tumor-associated factors governing progression from Tex_prog to Tex_term, however, are less established.

Tumor cells have long been regarded as direct sources of T cell dysfunction within the TME, and have likewise been a presumed source of the chronic antigen exposure promoting T cell exhaustion[23,24]. Here, we provide a detailed characterization of the progression from Tex_prog to Tex_term within the TME, where we observed a striking and disproportionate loss of Tex_prog over time in GBM, leading to a notably low progenitor exhaustion to terminal exhaustion ratio (PETER). We reveal that exhaustion is indeed concentrated within tumor-specific T cell subsets, with cognate antigenic exposure being requisite for acquisition of the Tex_term phenotype . However, we implicate tumor-associated macrophages (TAM), and not tumor cells, as the relevant source of antigenic exposure governing the Tex_prog to Tex_term transition. Using cell – cell interaction analsyis, we additionally highlight candidate TAM – T cell receptor/ligand communications that may be specifically mediating the progression to Tex_term and resultant decline in PETER within the TME.

# RESULTS

## GBM tumor-infiltrating lymphocytes (TIL) demonstrate a severe decline in the Progenitor Exhaustion to Terminal Exhaustion (PETE) Ratio over time

To better examine the dynamics of T cell exhaustion in GBM and other solid tumor models, but to eliminate any variables that might be imposed by anatomic compartment, we implanted murine GBM, melanoma, and lung (CT2A, B16F0, and LLC, respectively) tumor cells intracranially into syngeneic C57BL/6 mice, harvesting tumors when mice became moribund. We began by evaluating the frequency of both progenitor (Tex_prog) ($PD1^+Ly108^+TIM3^-$) and terminal (Tex_term) ($PD1^+Ly108^-TIM3+$) exhaustion in each model (**Figure 1A**). Consistent with our previous findings[6], GBM tumors demonstrated a higher frequency of Tex_term and correspondingly lower frequency of Tex_prog than the brain metastasis models (**Figure 1B and Supplemental Figure 1A**).

Having found that GBM possessed a particularly low progenitor exhaustion to terminal exhaustion ratio (which we have coined the PETE ratio, or PETER), we took this to indicate that GBM-infiltrating T cells may transition from Tex_prog to Tex_term at an especially high rate. We therefore selected GBM as an archetype tumor model to further examine the processes by which this transition occurs. To begin, we validated the expected transcriptional and functional differences across tumor-infiltrating Tex_prog and Tex_term from CT2A-bearing mice. We observed higher TOX expression in Tex_term compared to Tex_prog, with both subsets expressing higher expression than non-exhausted $PD1^-$ $CD8^+$ T cells, confirming the typical transcriptional landscape (**Figure 1C**). Likewise, upon PMA/Ionomycin stimulation *ex-vivo*, Tex_prog retained the ability to secrete IL2, IFN$\gamma$, and TNF$\alpha$, whereas Tex_term predominantly secreted IFN$\gamma$ alone (**Figure 1D**).

We next examined the evolution of T cell exhaustion within the tumor over time. We harvested CT2A tumors every 3 days from day 9 (D9) through D21 post-implantation, where mice were moribund at D21 (**Figure 1E**). T cell infiltration was observed within the tumor at D9, with substantial increases seen by D15 (**Figure 1F**). Furthermore, $CD8^+$ $PD1^+CD44^+$ T cells significantly increased in frequency from <20% on day 9 to >75% by D21 (**Figure 1G**). Within the $PD1^+CD44^+$ subset, we identified Tex_prog and Tex_term

as above, with transcriptional exhaustion confirmed via TOX expression **(Figure 1H**). Higher TOX levels were consistently seen in Tex_term than in Tex_prog at all timepoints in which both subsets were present (D12-21), confirming the anticipated pattern of expression (**Figure 1H**).

Importantly, Tex_prog was readily identifiable by D9 and accounted for ~60% of the $PD1^{+}CD8^{+}$ T cells found at the tumor, while Tex_term was notably absent at this early timepoint. The frequency of Tex_prog subsequently decreased over the course of tumor progression, accounting for less than 20% of $PD1^{+}CD8^{+}$ T cells by D21. (**Figures 1I and 1J**). Tex_term was identifiable starting D12 at low frequencies (~10%). By D21, however, Tex_term accounted for ~70% of $PD1^{+}CD44^{+}$ $CD8^{+}$ T cells (**Figures 1I and 1J**), further revealing a drop in PETER over time.

## scRNAseq defines transcriptional heterogeneity amongst GBM-infiltrating Tex_prog and Tex_term with an enrichment for cell-cell communication pathways in Tex_prog

To better understand the requirements for the transition from Tex_prog to Tex_term, we first performed scRNAseq on sorted $CD8^{+}$ T cells from glioma-bearing mice. Informed by our timecourse, we chose an earlier (D13) and a late (D19) timepoint for our analyses (**Figure 2A**). We identified six clusters of $CD8^{+}$ T cells, including two separate terminal exhaustion populations, which we termed Tex_term_early and Tex_term_late. While 5 of the clusters were present at both timepoints (D13 and 19), Tex_term_early was present only at D13 (**Figures 2B and 2C**). Clusters were annotated based on their top differentially expressed genes and their expression of known T cell exhaustion genes, namely *Tcf7*, *Tox*, and *Pdcd1* **(Figure 2D and Supplemental Figures 2A and 2B)**. Xcl1+_Tcm and Naïve-like clusters expressed memory/naïve T cell markers (*Sell, Il7r, Id3, Tcf7*), while Xcl1+_Tcm additionally expressed genes associated with activation and TCR signaling (*Xcl1, Klrk1, Nr4a2*) (**Figure 2D)**. The expression of *Pdcd1* and *Tox* on Tex_prog, Tex_int, Tex_term_early, and Tex_term suggested that these were T cell exhaustion subsets (**Figure 2D and Supplemental Figure 2B**). Tex_prog expressed effector (*Ifng, Tbx21*) and stem-like genes (*Cd28, Il7r, Tcf7, Tbx21*) and had a lower T cell exhaustion signature score (described by Im et al[19]) than Tex_int, Tex_term_early,

139 and Tex_term_late (**Figures 2D and 2E**). This could suggest that the exhaustion program
140 may not be fully established in Tex_prog. Next, Tex_int had increased expression of
141 exhaustion-associated genes (*Pdcd1, Tox, Entpd1*) and a decrease in effector (*Klrg1*)
142 and memory associated genes (*Tcf7, Il2*) (**Figure 2D**). Cytotoxicity-associated genes,
143 such as *Gzmb, Gzma*, and *Gzmk* were expressed at the highest levels in Tex_term_early
144 and Tex_term_late, consistent with previous characterization of terminal exhaustion[21]
145 (**Figure 2D**). Finally, Tex_term_late, predominantly found at the late timepoint and
146 consistent with our time-course characterizations, expressed the highest levels of
147 exhaustion-associated genes (*Pdcd1, Tox, Havcr2, Entpd1*) and lost *Tcf7* expression
148 (**Figure 2D and Supplemental Figure 2B**).

149 Once confident in our annotations, we employed pathway enrichment analysis for both
150 Tex_prog and Tex_term_late, which represented the two extreme ends of the exhaustion
151 pathway. This analysis revealed an abundance of pathways related to T cell migration,
152 differentiation, cell-cell communication and response to stimuli (cytokine, chemokines) in
153 Tex_prog (**Figures 2F and 2G**). This is in keeping with the current understanding of the
154 Tex_prog state and its prevalence among T cells entering or recently entering tumor [25,26].
155 In contrast, Tex_term were enriched for cytotoxic pathways, almost exclusively (**Figures**
156 **2F and 2G**). Importantly, this highlights that Tex_prog, unlike Tex_term, likely remain in
157 a signal-responsive state within the TME.

158 Lasty, we applied pseudotime analysis to our dataset to infer the temporal progression
159 amongst the T cell exhaustion subsets. This analysis spatially separated the Naïve_like
160 and Xcl1+_Tcm clusters from the other four clusters, supporting their identification as
161 separate, non-exhausted lineages (**Figure 2H**). The pseudotime plot ultimately validated
162 the progression from progenitor to terminal exhaustion through an intermediate
163 population (Tex_int). Interestingly, however, two trajectories were determined, both
164 beginning with Tex_prog (**Figure 2I**). While one ended with Tex_term_late, the other
165 ended in Tex_term_early. This finding is likely simply highlighting differences in
166 phenotypes for the predominant ending node at the early and late timepoints.

167 To further examine lineage relationships between the T cell exhaustion clusters, we
168 utilized our paired T cell receptor sequencing (TCRseq) dataset. To this end, we observed

169 TCR clonal overlap between predicted Tex clusters (**Figure 2J**). In combination with our
170 pseudotime results, this analysis suggests a trajectory of shared TCR clones, beginning
171 with Tex_prog, progressing through Tex_int and eventually ending with Tex_term. We
172 next compared clonal expansion between clusters, where we observed the greatest
173 frequency of "Large" expanded clones, (defined as between 20 and 100 cells with the
174 same clone), in Tex_term_late, and the lowest such frequency in Tex_prog (**Figure 2K**
175 **and 2L**). Correspondingly, Tex_prog had the greatest diversity index score, as measured
176 by the Shannon and Inverse Simpson indices, which has often been associated with
177 response to immunotherapy (**Supplemental Figure 2C**)[27]. Moreover, when we plotted
178 the 10 most expanded clones on a UMAP and divided the analysis by timepoint, we
179 observed that the expanded clones overwhelmingly resided in Tex_int, Tex_term_early
180 and Tex_term_late, but not Tex_prog (**Supplemental Figure 2D**). This suggests that
181 clonal expansion in response to TCR stimulation closely reflects T cell exhaustion
182 progression.

183

184 **Tumor cells are not a necessary source of the TCR stimulation mediating**
185 **Tex_prog to Tex_term transition**

186 In light of the above observations, we hypothesized that antigen-specific TCR activation
187 would be required for progression of Tex_prog to Tex_term within the TME, and thus that
188 Tex_term would be concentrated amongst tumor-specific T cells. To test this directly, we
189 employed a model in which CT2A gliomas were engineered to express the antigen TRP2
190 (See STAR Methods). We then adoptively transferred either tumor-specific TRP2 TCR-
191 transgenic $CD8^+$ T cells (TRP2-TCR) or irrelevant OVA antigen-specific (OT1) $CD8^+$ T
192 cells into CT2A-TRP2-bearing mice (**Figure 3A**). All T cells were activated *ex vivo* prior
193 to transfer. Two weeks later, tumors were harvested, and adoptively transferred T cells
194 were identified as TRP2 $tetramer^+CD45.1^+$ (TRP2-TCR) or OVA $tetramer^+$ (OT1) and
195 evaluated for exhaustion phenotypes. Unsurprisingly, recovery of TRP2-TCR T cells from
196 tumor was significantly better than recovery of OT1 T cells (**Figure 3B**). Recovered TRP2-
197 TCR T cells also demonstrated significantly higher acquisition of a Tex_term phenotype
198 than OT1 T cells, which only minimally acquired PD1 expression (**Figures 3C and 3D**
199 **and Supplemental Figure 3A**). Unlike OT1 T cells, transferred TRP2-TCR T cells

200 developed into predominantly Tex_int and Tex_term, similar to endogenous tumor-
201 specific T cells (TRP2 tetramer$^{+}$CD45.2$^{+}$) (**Supplemental Figure 3B)**. Taken together,
202 these data strongly suggest that T cells in the TME must encounter their cognate antigen
203 to progress along the exhaustion pathway and complete the transition to Tex_term.

204 As tumor antigen-specific TCR stimulation appeared to be necessary for exhaustion
205 progression, we first supposed that the relevant antigen-cognate interaction would be
206 between T cells and tumor cells. To evaluate this, we compared the progression of T cell
207 exhaustion *in vivo* within CT2A-TRP2 and CT2A-TRP2-β2mKO tumors, where the latter
208 constitutes a cell line where β2m is knocked out using CRISPR-Cas9 (See STAR
209 Methods). Knockout of β2m leaves the tumor without the capacity to build functional MHC
210 I molecules, and thus without the capacity to present antigen to T cells (**Figure 3E and**
211 **Supplemental Figure 3C**). Surprisingly, we observed no significant difference in the
212 frequency of PD1$^{+}$ TRP2-TCR T cells or in the frequency of T cell exhaustion subsets
213 (Tex_prog or Tex_term) in the absence of tumor MHC I expression and antigen
214 presentation (**Figures 3F, 3G, and 3H**). Of note, the extent of T cell infiltration was
215 comparable between MHC I expressing and non-expressing tumors (**Supplemental**
216 **Figure 3D**).

217

## 218 TAM are the most frequent and most potent cross-presenting antigen-
## 219 presenting cells (APC) within the intracranial TME

220 With tumor cells seemingly eliminated as the source of exhaustion-relevant antigen-
221 cognate interactions with T cells, we next sought to narrow down additional candidate
222 antigen presenting populations. We therefore evaluated other sources of potentially
223 determinant antigen-cognate interactions within the TME. Such relevant APC might
224 include monocytes, TAM, microglia, and/or dendritic cells (DC)[28]. Using a scRNAseq
225 dataset of CD45$^{+}$ cells sorted from CT2A tumors previously published by our group[29], we
226 identified predicted sources of MHC I cell-cell interactions in the TME. We isolated a
227 component of the dataset that included the above APC types and CD8$^{+}$ T cells, then
228 conducted cell-cell interaction analysis using the CellChat pipeline[29,30] (Schematic in
229 **Figure 4A**). Importantly, MHC I signaling was a highly predicted interaction between T
230 cells and all potential APC (**Figure 4B**). This analysis revealed the greatest *number* of

231 predicted interactions between CD8$^+$ T cells and Apoe$^+$ TAM, while the *strength* of
232 predicted interactions was similar across APC (**Figure 4C and Supplemental Figure**
233 **4A**). Notably, TAM greatly outnumber other APC in the CT2A TME, comprising ~40% of
234 tumor-infiltrating immune cells (**Figure 4D**). Combined, these results suggested that the
235 relevant antigen-cognate interactions promoting exhaustion progression within the TME
236 are occurring between CD8$^+$ T cells and APC (and not tumor), with TAM being the the
237 most abundant source of antigen.

238 To investigate the relevant antigen-presenting functions of the various APC subtypes
239 within CT2A, we directly evaluated their relative *in vivo* phagocytic activity within the TME.
240 To this end, we implanted GFP-expressing CT2A tumors and evaluated the frequency of
241 GFP positivity within intratumoral APC when mice were moribund (schematic in **Figure**
242 **4E**). We focused on monocytes (CD11b$^+$F4/80$^+$Ly6C$^{hi}$), TAM (CD11b$^+$F4/80$^+$MHC II$^+$),
243 DC (F4/80$^-$CD11c$^+$MHC II$^+$), and microglia (CD45$^{int}$CD11b$^+$F4/80$^+$) (**Supplemental**
244 **Figure 4B**). We found that monocytes, TAM, and DC all took up GFP (**Figure 4F**). After
245 phagocytosing exogenous antigen, APC must load and cross-present the antigen via
246 MHC I to interact with CD8 T cells[31]. We therefore next probed for differential MHC I
247 expression as a surrogate for subsequent tumor antigen cross-presentation. TAM and
248 DC both had significantly higher MHC I on their surface than other APC populations
249 (**Figures 4G and 4H**).

250 To more directly evaluate the cross-presentation capacity of intratumoral APC, we
251 implanted OVA-expressing CT2A tumors and subsequently assessed the various APC
252 populations by flow cytometry for the presence of SIINFEKL-loaded MHC I (Schematic in
253 **Figure 4I**). Among APC, we observed the greatest frequency of SIINFEKL-loaded MHC
254 I on TAM and their monocyte precursors (**Figure 4J**). Combining our data, then, TAM
255 appeared to exhibit the greatest potency for both phagocytosing and cross-presenting
256 tumor antigen within the TME.

257

## 258 TAM mediate progenitor to terminal exhaustion transition in GBM and other 259 solid tumor models

260 To better establish the requirement for TAM in the progression from Tex_prog to
261 Tex_term, we implanted CT2A tumors into CCR2KO mice. CCR2KO mice exhibit

262 impaired monocyte trafficking toward sites of inflammation[32], therefore establishing a
263 TME that is relatively deficient in TAM, which are monocyte-derived. To further the extent
264 of TAM depletion in this model, however, we also administered tumor-bearing CCR2KO
265 mice an anti-CSF1R antibody, which eliminates differentiated TAM (schematic in **Figure**
266 **5A**)[33]. We observed efficient depletion of TAM with this approach (**Supplementary**
267 **Figure 5A**). Importantly, there was a significant increase in PETER observed in the
268 CCR2KO setting (**Figures 5B and 5C**), suggesting a relative failure to progress from
269 Tex_prog to Tex_term. Notably, we likewise observed a strong positive correlation
270 between the frequency of Tex_term and the frequency of TAM remaining within the TME,
271 as Tex_term proportions dropped substantially with improved TAM depletion (**Figure 5D**).
272 Importantly, we did not observe similar alterations to PETER when we depleted DC
273 (**Figure 5E and 5F**) or microglia (**Figure 5G and 5H) (Supplemental Figures 5B-5E**),
274 further suggesting TAM as the pertinent APC population for driving the progression of T
275 cell exhaustion in this model.

276 With these observations, we next evaluated the role of MHC I presentation by TAM in
277 driving progression of T cell exhaustion. To this end, we generated β2m bone marrow
278 chimeras (β2mKO donors into WT recipients), wherein hematopoietic cells (including
279 hemaptopoietically-derived APC) lacked β2m and antigen presenting capacity (see STAR
280 Methods). While we continued to observe low levels of MHC I expression on TAM in this
281 model, likely as a result of TAM trogocytosis of MHC I from surrounding β2m-replete
282 cells[34] (**Supplemental Figures 5F and 5G**), we observed a positive correlation between
283 persisting MHC $I^+$ on TAM and the frequency of Tex_term (**Figure 5I**).

284 These findings in CT2A raised the question as to whether the role of TAM in driving
285 exhaustion progression was exclusive to GBM and/or to the intracranial environment. To
286 assess this, we employed the same TAM depletion approach in both orthotopic and
287 intracranial murine models of melanoma (schematic in **Figure 5J**). As before, we saw
288 efficient depletion of TAM (**Supplementary Figures 5H and 5I**). Importantly, in both
289 peripheral and intracranial melanoma models, we observed a significant increase in
290 PETER within the TME in the setting of TAM depletion (**Figures 5K-5N**). These findings
291 implicate TAM as a primary source of tumor-antigen presentation mediating T cell

292 exhaustion progression across multiple solid tumor types and locations. Taken together,
293 these data suggest Tex_prog progresses to Tex_term independently of tumor-derived
294 antigen presentation, and instead requires antigen-cognate interactions between T cells
295 and antigen cross-presenting APC, with TAM being the most relevant of these.

296

## 297 CellChat predicts secondary interactions between TAM and CD8$^+$ T cells in 298 mice and humans that may contribute to exhaustion progression

299 Given the above role uncovered for TAM, we returned to the cell – cell interaction analysis
300 from Figure 3 to further interrogate interactions between TAM and Tex_prog that might
301 be contributors to Tex_prog progression to Tex_term (schematic in **Figure 6A**). Several
302 TAM ligands or surface molecules were highlighted in our scRNAseq dataset, with
303 pathways ranging from inhibitory (PD-L1, SPP1, GALECTIN) to stimulatory (CD86), to
304 cell-cell adhesion (ICAM, JAM) to migration (CXCL), among others (**Figure 6B**). We
305 further refined these possibilities by selecting receptors/ligands that were expressed in
306 our scRNAseq dataset and specifically present in the Tex_prog cluster (**Figure 6C**). From
307 these analyses, we observed that cell – cell adhesion (*Itgb1, Itgb2, Itga4*), migration
308 (*Cxcr3*) and stimulatory molecules (*Cd28*) were particularly enriched in Tex_prog
309 compared to Tex_term, consistent with the pathways identified in Figure 2F. Tex_term,
310 by comparison, had greater expression of inhibitory receptors (*Pdcd1, Ctla4, Tigit*) and
311 the chemokine receptor, *Cxcr6*.

312 To determine which of the above predicted interactions might also be prevalent in
313 patients, we turned to publicly available human GBM and metastatic melanoma datasets.
314 We integrated 15 newly diagnosed GBM (ndGBM) and 5 treatement-naïve metastatic
315 brain melanoma (MBM) samples and focused on TAM and CD8$^+$ T cells for further
316 analysis[35,36]. Once integrated, we derived 8 TAM clusters and 3 CD8 clusters that were
317 shared between tumor types (**Figure 6D**). As expected, the abundance of TAM was
318 greater in ndGBM than in MBM (**Figure 6E**). We then performed cell – cell communication
319 analysis with the human samples using CellChat as previously described[30]. Broadly, we
320 noted that CD8$^+$ T cells possessed high "incoming interaction" levels but low "outgoing
321 interaction" strength for both tumor types, whereas TAM had comparable
322 incoming/outgoing strengths, highlighting their interconnectedness within the TME

323 (**Figure 6F**). The total interaction strength was much higher in MBM than ndGBM,
324 suggesting the MBM TME, as a whole, exhibits receptor – ligand pairs at a higher level
325 (**Figure 6F**).

326 Given the higher strength of incoming interactions amongst $CD8^+$ T cells, we evaluated
327 which predicted interactions were prevalent between TAM and $CD8^+$ T cells across tumor
328 types. Among those predicted, several overlapped with our CellChat analysis of murine
329 GBM, including MHC-I, SPP1, CD86, ICAM, FN1, JAM, CXCL, and GALECTIN (**Figures**
330 **6B and 6G**). Interestingly, ndGBM was primarily enriched for cell – cell adhesion
331 interactions, whereas MBM had exhibited a greater representation of
332 inflammatory/migration pathways. These results align with perceptions of GBM as an
333 "immunologically cold" tumor compared to MBM[37,38]. When comparing the intensity of
334 these pathways between tumor types, we again observed an increased strength and
335 number of interactions in the MBM group (**Figure 6H**). Notably, the SPP1 and FN1
336 pathways were significantly upregulated in the ndGBM samples compared to MBM.
337 These findings highlight enriched interactions between TAM and $CD8^+$ T cells that may
338 be implicated in T cell exhaustion progression across tumor types, tumor locations, and
339 species, thus warranting further investigation.

# 340 DISCUSSION

341 The abundance of Tex_prog within a TME is currently believed to reflect
342 immunotherapeutic responsivity [15,21,22,38,39]. Initially identified as the T cell differentiation
343 state remaining reactive to anti-PD1 treatment in chronic infection, Tex_prog has now
344 been recognized as a consistent correlate of ICB response[15,19,20]. Some studies have
345 further identified the abundance of Tex_prog relative to Tex_term as critical[22]. Here, we
346 detail the severe and disproportionate loss of Tex_prog over time in GBM and other solid
347 tumors and implicate TAM, but not tumor cells, as the mediators of the Tex_prog to
348 Tex_term transition. Recognizing the importance of this shift from Tex_prog to Tex_term,
349 we, in turn, coin and identify the PETER as an important indicator of the dynamics of T
350 cell exhaustion within the TME. As GBM possesses a particularly low PETER and is
351 likewise unresponsive to immune checkpoint blockade, we suggest that a therapeutic
352 goal for licensing improved immunotherapeutic responses may ultimately be finding ways

353 to optimize PETER within a given TME .

354 Further characterizing Tex_prog and Tex_term, we observe an enrichment for
355 chemotactic and cell-cell adhesion pathways in Tex_prog, and we implicate TAM as
356 driving a subsequent loss of T cell polyfunctionality and stem-like properties as T cells
357 increasingly differentiate toward Tex_term in tumor. In the absence of TAM, we instead
358 observe retention of the Tex_prog population and a resultant increase in PETER, with the
359 retained Tex_prog possessing established implications for immunotherapeutic
360 responsivity[16,19-22].

361 Until recently, most defining studies for T cell exhaustion have been conducted in a
362 chronic infection model of lymphocytic choriomeningitis virus (LCMV)[14,17,40]. In the LCMV
363 model, it is unfortunately impossible to determine whether T cell chronic antigen exposure
364 occurs on the surface of infected target cells or APC, as they are typically one and the
365 same. As a result, a common presumption is that chronic exposure to antigen presented
366 by target cells is a driver of T cell exhaustion progression. In contrast, in tumors, T cell
367 antigen exposure may occur on the surface of tumor cells presenting endogenous
368 antigen, or in the context of TME APC cross-presenting exogenous antigen. Looking to
369 assess whether one antigenic context might be more crucial to the derivation of
370 exhaustion in the TME, we removed the capacity for MHC I presentation from tumor cells
371 and observed no change in the frequency of T cell exhaustion subsets. This suggested
372 that encountering antigen on tumor cells is not required for the differentiation of Tex_prog
373 to Tex_term, leaving intratumoral APC as our next-investiagted source of instigatory
374 antigen-cognate interactions.

375 In our intial querying of intratumoral APC, DC were a leading logical candidate for
376 exhaustion-eliciting interactions with Tex_prog. Surprisingly, however, interactions with
377 DC, although present, proved to be neither necessary nor sufficient for the differentiation
378 of Tex_prog to Tex_term. Rather, we found that both TAM and TAM MHC I are necessary
379 components. Importantly, in addition to being the most abundant APC, TAM also
380 demonstrated the greatest propensity for phagocytosis and cross-presentation in the
381 TME. The sheer number of predicted TAM – T cell interactions are important as they are
382 generally only weakly activating and often even immunosuppressive compared to DC –

383 T cell interactions[28,41-43]. Our findings, however, highlight a previously unappreciated
384 immunoregulatory role for TAM and provide a new focus on determining relevant T cell
385 – TAM interactions for targeting in an effort to better license immunotherapeutic
386 responses.

387 While antigen cognate interactions with TAM may be a necessary first step in driving T
388 cell exhaustion within the TME, our data suggest that there are additional secondary
389 interactions that follow that may more proximally mediate the Tex_prog to Tex_term
390 transition. Other groups have proposed co-stimulatory signals through the CD86/CD28
391 axis as contributors[26]. Our CellChat findings suggest that such interactions may indeed
392 play a role in more inflammatory tumors, such as MBM, but this axis was not prevalent in
393 our human ndGBM dataset. Interestingly, we identified SPP1, which binds to integrins
394 (CD44 or CD29) on $CD8^+$ T cells, as a highly predicted component of interaction between
395 TAM and $CD8^+$ T cells in in both murine and human tumors. Importantly, SPP1 has
396 recently been ascribed a T cell exhaustive role in the setting of GBM. Kilian *et al.* identified
397 a pathway in which the absence of $CD4^+$ T cell – TAM MHC II interactions led to increased
398 secretion of SPP1 by TAM, which suppressed surrounding $CD8^+$ T cells and increased
399 their expression of exhaustion-associated factors[44]. Further studies are ultimately needed
400 to better address the nature and role of specific interactions between TAM and $CD8^+$ T
401 cells.

402 Taken together, we have highlighted TAM – T cell interactions as critical for driving $CD8^+$
403 T cell exhaustion progression in GBM and other solid tumors. Future work will focus on
404 defining specific TAM – T cell interactions and their relative contributions to the
405 differentiation of Tex_prog to Tex_term. The goal remains to promote a TME with a
406 heightened PETER and renewable Tex_prog populations in an effort to better license
407 immunotherapeutic responses.

408

409

410 ## ACKNOWLEDGMENTS

411 Dr. Fecci, and the research contained herein, is supported by a Cancer Research Institute
412 Lloyd J Old STAR award. We would like to thank the Duke Molecular Genomics Core,
413 Duke Human Vaccine Institute Flow Cytometry Core, and the Duke Cancer Institute Flow
414 Cytometry Core.

415 ## AUTHOR CONTRIBUTIONS

416 Conceptualization, J.WP and P.E.F.; Methodology, J.WP., W.H.T., A.M.H-M., L.P.W.,
417 D.S.W., E.L., and K.W.; Investigation, J.WP.; Resources, J.WP., W.H.T., A.M.H-M., and
418 J.B.F.; Writing – Original Draft, J.WP.; Writing – Review & Editing, J.WP., A.M.H-M.,
419 W.H.T., L.P.W., S.J.L. and P.E.F.; Supervision, P.E.F.; Funding Acquisition, J.WP., and
420 P.E.F.

421 ## DECLARATIONS OF INTEREST

422 The authors declare no competing interests.

423 # FIGURE TITLES and LEGENDS

424 Figure 1: GBM tumor-infiltrating lymphocytes (TIL) demonstrate a severe decline in the
425 Progenitor Exhaustion to Terminal Exhaustion (PETE) Ratio over time.

426 (A) Representative contour plots of Tex_prog and Tex_term across tumor types.

427 (B) PETER across CT2A, B16F0 and LLC intracranial tumors, harvested when mice were
428 moribund. n = 8-10 mice/group.

429 (C and D) Geometric mean fluorescence intensity (gMFI) of intracellular TOX expression
430 (C) and quantification of TNFa/IFNy/IL2 of Tex_prog and Tex_term in 10K CT2A at D18
431 (D). n = 5 mice. Representative of two independent experiments.

432 (E) Experimental layout. 10K CT2A cells implanted D0, tumors were harvested every 3
433 days starting D9 until mice were moribund on D21. Created with Biorender.

434 (F) number of CD8+ T cells per harvested tumor. n = 5 mice/timepoint.

435 (G) Frequency of $PD1^{+}CD44^{+}$ of $CD8^{+}$ T cells. n = 5 mice/timepoint.

436 (H) Geometric mean fluorescence intensity (gMFI) of TOX of Tex_prog and Tex_term
437 across timepoints with >100 total $PD1^{+}CD44^{+}$ $CD8^{+}$ T cells. n = 5 mice/timepoint.

438 (I and J) Representative plots showing Ly108 vs. TIM3 progression from D9 to D21,
439 Tex_prog = top left, Tex_int = bottom left, Tex_term = bottom right (I) and quantification
440 of Tex subsets of PD1+CD44+ CD8+ T cells over time (J). n = 5 mice/timepoint.

441 All of the data are means ± SEMs; p-values are shown on individual plots as determined
442 by 1-way ANOVA and post-hoc Tukey test (A, F, G), two-sided paired t-test (B) or RM 2-
443 way ANOVA and post-hoc Tukey test (D and H). See also Figure S1.

444

445 Figure 2: scRNAseq defines transcriptional heterogeneity amongst GBM-infiltrating
446 Tex_prog and Tex_term with an enrichment for cell-cell communication pathways int
447 Tex_prog.

448 (A) Experimental layout for scRNAseq experiment. tumors were harvested at an early
449 (D13) and late (D19) timepoint. Created with Biorender.

450 (B) UMAP of 6 CD8 T cell clusters following QC.

451 (C) Frequency of each cluster per timepoint. (D) Heatmap of exhaustion associated
452 transcription factors, cytokines/secreted molecules, and surface markers.

453 (E) AddModuleScore of exhaustion signature from Im et al., 2016, violin plot and density
454 plot representations.

455 (F) Significantly upregulated pathways in Tex_prog and Tex_term from Hallmark,
456 Reactome, Gene Ontology databases.

457 (G) Relevant genes from upregulated pathways in F.

458 (H) Trajectory analysis overlaid onto clusters from B.

459 (I) Trajectory analysis overlaid onto pseudotime.

460 (J) Circle plot of overlapping clones across Tex_clusters. Tex_prog, Tex_int have
461 overlapping clones with all other clusters. Tex_term and Tex_int_2 do not have
462 overlapping clones.

463 (K) UMAP of cloneTypes across clusters.

464 (L) Frequency of cloneTypes across clusters.

465 See also Figure S2.

466

467 Figure 3: Tumor cells are not a necessary source of the TCR stimulation mediating
468 Tex_prog to Tex_term transition

469 (A) Experimental layout. 250K *ex-vivo* activated and transduced OT1 and TRP2-TCR T
470 cells were intracranially implanted into D7 CT2A-TRP2-bearing mice. Tumors were
471 harvested 14 days later.

472 (B) Frequency of implanted cells recovered on D21. n = 7 mice/group.

473 (C and D) Frequency of PD1+ CD8+ T cells in OT1 vs. TRP2-TCR (C) and representative
474 contour plot PD1 and TIM3 expression of OT1 and TRP2-TCR T cells 14 days post-
475 transfer (D). n = 7 mice/group

476 (E) Experimental layout. 50K CT2A-TRP2 or CT2A-TRP2-B2mKO were implanted

477 intracranially and harvested when mice were moribund. Created with Biorender.

478 (F) Frequency of PD1+ TRP2-TCR T cells between groups. n = 10 mice/group.

479 (G and H) Frequency of Tex subset of PD1+TRP2-Tetramer+ CD8+ T cells and
480 representative contour plot (G) and representative contour plot of Ly108 and TIM3
481 expression between groups (H). n = 10 mice/group.

482 All of the data are means ± SEMs; p-values are shown on individual plots as measured
483 by two tailed t-test (B, C, F) or RM 2-way ANOVA (G). See also Figure S3.

484

485 Figure 4: TAM are the most frequent and most potent cross-presenting antigen-
486 presenting cells (APC) within the intracranial TME.

487 (A) Experimental layout. CD45+ sorted scRNAseq from Tomaszewski et al., 2022 was
488 analyzed with CellChat to determine which APC had predicted MHC I interactions with
489 CD8 T cells. Created with Biorender.

490 (B) Heatmap showing communication probability of MHC I interactions in the TME. All
491 APC were predicted to interact with CD8 TIL through MHC I.

492 (C) Circle plot displaying number of interactions (thickness of arrow/number) across APC
493 populations.

494 (D) Frequency of infiltrating immune cells from Tomaszewski et al., 2022 dataset.

495 (E) Experimental layout. 25K CT2A-GFP was implanted intracranially and harvested
496 when mice were moribund. GFP+ APC were evaluated. Created with Biorender.

497 (F) Frequency of GFP+ T cells ($CD3^+$), TAM ($CD45^{hi}CD11b^+F4/80^+$), DC ($CD11b^+$MHC
498 $II^+F4/80^-$) and Microglia ($CD45^{hi}CD11b^+F4/80^+$). n = 5 mice.

499 (G and H) gMFI of MHC I of APC populations from F (G) and representative histogram
500 (H). n = 5 mice.

501 (I) Experimental layout. 100K CT2A-OVA was implanted intracranially and harvested
502 when mice were moribund.

503 (J) Frequency of SIINFEKL-loaded MHC I of T cells, TAM, Monocytes

504 (CD11b+F480$^{int}$Ly6C$^{hi}$), DC, and Microglia. n = 9 mice.

505 p-values are plotted on individual graphs. Statistical significance was determined by 1-
506 way ANOVA (F, G, J) with post-hoc Tukey's test for multiple comparisons. All data are
507 plotted as mean ± SEM. See also Figure S4.

508

509 Figure 5: TAM mediate progenitor to terminal exhaustion transition in GBM and other
510 intracranial solid tumor models.

511 (A) Experimental layout. TAM and monocytes were depleted in CCR2KO mice with
512 aCSF1R depletion antibody. 10K CT2A was implanted intracranially and harvested when
513 mice were moribund. Created with Biorender.

514 (B and C) Frequency of Tex_subsets of PD1+CD44+ (B) and PETER between WT and
515 TAM depleted groups (C). Data pooled from 2 independent experiments. n = 10-11
516 mice/group.

517 (D) Simple linear correlation of %Tex_term of PD1+CD44+ CD8+ T cells vs. % TAM of
518 CD45+. Data pooled from 2 independent experiments. n = 11 mice/group.

519 (E and F) CD11c+ DC were depleted with 5ng/g DTR injections on D8, D11, D14, D17
520 post CT2A-implantation. Frequency of T cell exhaustion subsets (E) and and PETER
521 between WT and DC depleted groups (F). n = 5 mice/group.

522 (G and H) Microglia were depleted with 290mg/kg PLX3397 free-fed chow starting 1 week
523 prior to CT2A implantation. Frequency of T cell exhaustion subsets (G) and PETER
524 between WT and microglia depleted groups (H). n = 10 mice/group.

525 (I) Simple linear correlation of frequency of Tex_term vs. Frequency of MHC I+ TAM in
526 B2mKO chimera mice implanted with CT2A.

527 (J) Experimental layout. TAM and monocytes were depleted in CCR2KO mice with
528 aCSF1R depletion antibody. 1K B16F0 was implanted intracranially or 100K B16F0 was
529 implanted subcutaneously and harvested when mice were moribund. Created with
530 Biorender.

531 (K and L) Frequency of Tex_subsets of PD1+CD44+ B16F0 IC (K) and PETER between

532 WT and TAM depleted groups (L). n = 9-10 mice/group.

533 (M and N) Frequency of Tex_subsets of PD1+CD44+ B16F0 SQ (M) and PETER
534 between WT and TAM depleted groups (N). Data pooled from 2 independent
535 experiments. n = 6-7 mice/group.

536 p-values are plotted on individual graphs. Statistical significance was determined by two-
537 sided unpaired t test (C, F, H, L, N) or RM-2-way ANOVA with post-hoc Tukey's test for
538 multiple comparisons (B, E, G, K, M). All data are plotted as mean ± SEM. See also Figure
539 S5.

540

541 Figure 6: CellChat predicts secondary interactions between TAM and $CD8^+$ T cells in mice
542 and humans that may contribute to exhaustion progression

543 (A) Experimental layout. CD45+ sorted scRNAseq from murine GBM, ndGBM and MBC
544 was analyzed with CellChat to determine additional TAM-T cell interactions. Created with
545 Biorender.

546 (B) Enriched predicted interactions with TAM (orange) as the source and CD8 TIL (blue)
547 as the target from murine GBM.

548 (C) Receptors expression in Tex_prog vs. Tex_term from CD3+ sorted dataset from
549 Figure 2 of predicted interactions from 6B.

550 (D) UMAP of human ndGBM and MBM datasets.

551 (E) Frequency of TAM vs. CD8s in ndGBM vs. MBM.

552 (F) Incoming vs. outgoing interaction strength across cell types in ndGBM vs. MBM.

553 (G) Heatmap of all incoming signaling patterns in ndGBM vs. MBM.

554 (H) Significantly upregulated predicted pathways in ndGBM (maroon) vs. MBM (grey).

555

556

557 # TABLES with TITLES and LEGENDS

558 **Table S1: Exhaustion signature (Im et al. 2016)**

| |
|---|
| *Pdcd1* |
| *Tox* |
| *Il21r* |
| *Sh2d2a* |
| *Cd8a* |
| *Nkg7* |
| *Fgl2* |
| *Entpd1* |
| *Fasl* |
| *Ccl5* |
| *Apol7e* |
| *Arhgap9* |
| *Nedd9* |
| *Cd38* |
| *Pvrig* |
| *Trbc2* |
| *Chn2* |
| *2900026A02Rik* |
| *Pstpip1* |
| *Chst12* |
| *Cd3e* |
| *Cxcr6* |
| *Cd3g* |
| *Adgrg1* |
| *Prkch* |
| *Tap2* |
| *Irf1* |
| *Tapbpl* |
| *AW112010* |
| *Arl6ip1* |
| *Gng2* |
| *Adam19* |
| *Gimap7* |
| *Gzmk* |

559

560 # STAR METHODS

561 ## Key Resources Table

| Reagent or Resource | Source | Identifier |
|---|---|---|
| Antibodies | | |
| anti-mouse anti-GFP - Alexa Fluor® 488 (clone FM264G) | Biolegend | Cat# 338008; RRID:AB_2563288 |
| anti-mouse CD11b - APCR700 (clone M1/70) | BD Biosciences | Cat# 564985; RRID:AB_2739033 |
| anti-mouse CD11c - BV421 (clone N418) | BD Biosciences | Cat# 565452; RRID:AB_2744278 |
| anti-mouse CD16/32TruStain FcX™ (clone 93) | Biolegend | Cat# 101320; RRID:AB_1574975 |
| anti-mouse CD19 - Alexa Fluor® 488 (clone 6D5) | Biolegend | Cat# 115521; RRID:AB_389307 |
| anti-mouse CD24 - Brilliant Violet 605™ (clone M1/69) | Biolegend | Cat# 101827; RRID:AB_2563464 |
| anti-mouse CD3 - APC (clone 145-2C11) | Biolegend | Cat# 100312; RRID:AB_312677 |
| anti-mouse CD3 - PECy5 (clone 145-2C11) | Biolegend | Cat# 552774; RRID:AB_394460 |
| anti-mouse CD3 - PECy7 (clone 145-2C11) | Biolegend | Cat# 100310; RRID:AB_312675 |
| anti-mouse CD39 - PE-eFluor610 (clone 24DMS1) | Invitrogen | Cat# 61-0391-82; RRID:AB_2848486 |
| anti-mouse CD39 - PECy7 (clone 24DMS1) | Invitrogen | Cat# 61-0391-82; RRID:AB_2848486 |
| anti-mouse CD44 - Brilliant Violet 785™ (clone IM7) | Biolegend | Cat# 103059; RRID:AB_2571953 |
| anti-mouse CD44 - PE-CF594 (clone IM7) | BD Biosciences | Cat# 562464; RRID:AB_11153123 |
| anti-mouse CD45 - APCCy7 (clone 30-F11) | Biolegend | Cat# 103116; RRID:AB_312981 |

| | | |
|---|---|---|
| anti-mouse CD45 - BV605 (clone 30-F11) | Biolegend | Cat# 103155; RRID:AB_2650656 |
| anti-mouse CD45.1 - Alexa Fluor® 488 (clone A20) | Biolegend | Cat# 110718; RRID:AB_492862 |
| anti-mouse CD45.1 - PECy7 (clone A20) | BD Biosciences | Cat# 110730; RRID:AB_1134168 |
| anti-mouse CD45.2 - APCCy7 (clone 104) | Biolegend | Cat# 109824; RRID:AB_830789 |
| anti-mouse CD86 - Brilliant Violet 650™ (clone GL-1) | Biolegend | Cat# 109824; RRID:AB_830789 |
| anti-mouse CD8a - APCR700 (clone 53-6.7 | BD Biosciences | Cat# 564983; RRID:AB_2739032 |
| anti-mouse CX3CR1 - APC (clone SA011F11) | Biolegend | Cat# 149007; RRID:AB_256449 |
| anti-mouse CX3CR1 - APC (clone SA011F11) | Biolegend | Cat# 149006; RRID:AB_2564315 |
| anti-mouse F4/80 - PECy5 (clone BM8) | Invitrogen | Cat# 15-4801-82; RRID:AB_468798 |
| anti-mouse H2Kb bound to SIINFEKL - PE (clone 25-D1.16) | Biolegend | Cat# 141604; RRID:AB_10895905 |
| anti-mouse H2Kb/H2Kd - PECy7 (clone 28-8-6) | Biolegend | Cat# 114616; RRID:AB_2750196 |
| anti-mouse IA/IE - Brilliant Violet 785™ (clone M5/114.15.2 | Biolegend | Cat# 107645; RRID:AB_2565977 |
| anti-mouse IFNγ - PE/Dazzle 594 (clone XMG1.2) | Biolegend | Cat# 505846; RRID:AB_2563980 |
| anti-mouse IFNγ - Alexa Fluor® (clone XMG1.2) | Invitrogen | Cat# 53-7311-82; RRID:AB_469932 |
| anti-mouse IL2 - Brilliant Violet 785™ (clone JES6-5H4) | Biolegend | Cat# 503843; RRID:AB_2832801 |
| anti-mouse Ki67 - BV785 (clone B56) | BD Biosciences | Cat# 563756; RRID:AB_2732007 |
| anti-mouse Ki67 - PECy7 (clone B56) | BD Biosciences | Cat# 561283; RRID:AB_10716060 |
| anti-mouse KLRG1 - PECy5 (clone 2F1) | Invitrogen | Cat# 15-5893-80; RRID:AB_2811751 |

| | | |
|---|---|---|
| anti-mouse Ly108 - BV650 (clone 13G3) | BD Biosciences | Cat# 740628; RRID:AB_2740323 |
| anti-mouse Ly108 - BV786 (clone 13G3) | BD Biosciences | Cat# 741030; RRID:AB_2740648 |
| anti-mouse Ly6C - PE (clone HK1.4) | Biolegend | Cat# 128007; RRID:AB_1186133 |
| anti-mouse MHC I Tetramer H2Kb OVA - PE | MBL | Cat# TB-5001-1 |
| anti-mouse MHC I Tetramer H2Kb TRP2 - PE | MBL | Cat# TB-5004-1 |
| anti-mouse PD1 - Brilliant Violet 711™ (clone 29F.1.A12) | Biolegend | Cat# 135231; RRID:AB_2566158 |
| anti-mouse TCF1 - PE (clone S33-966) | BD Biosciences | Cat# 564217; RRID:AB_2687845 |
| anti-mouse TCR Vβ3 - BV605 (clone KJ25) | BD Biosciences | Cat# 743414; RRID:AB_2741487 |
| anti-mouse TCR Vβ3 - PE (clone KJ25) | BD Biosciences | Cat# 553209; RRID:AB_394709 |
| anti-mouse TIM3 - Brilliant Violet 421™ (clone RMT3-23) | Biolegend | Cat# 119723; RRID:AB_2616908 |
| anti-mouse TNFα - APC (clone MP6-XT22) | Biolegend | Cat# 506308; RRID:AB_315429 |
| anti-mouse TNFα - Brilliant Violet 785™ (clone MP6-XT22) | Biolegend | Cat# 506341; RRID:AB_2565951 |
| anti-mouse TOX - eFluor660 (clone TXRX10) | Invitrogen | Cat# 50-6502-82; RRID:AB_2574265 |
| Biologic Samples | | |
| Mouse tissue samples (brain tumor, spleen) | Duke University | IACUC: A163-21-08 |
| | | |
| Buffers, chemicals, and recombinant proteins | | |
| 0.05% Trypsin-EDTA | GIBCO | Cat# 25300-054 |
| 2-Mercaptoethanol | GIBCO | Cat# 21985023 |
| BD Golgiplug™ (Brefeldin A) | BD Biosciences | Cat# 555029 |
| BD Golgiplug™ (Brefeldin A) | BD Biosciences | Cat# 554724 |
| Concanavalin A (Con A) Solution (500X) | eBioscience | Cat# 00-4978-93 |

| | | |
|---|---|---|
| CountBright Absolute Counting Beads | Invitrogen | Cat# C36950 |
| DMEM | GIBCO | Cat# 11965118 |
| DnaseI | Sigma-Aldrich | Cat# 10104159001 |
| Fetal Bovine Serum (FBS) | Sigma | Cat# F4135 - 500mL |
| Foxp3/Transcription factor staining buffer set | eBioscience | Cat# 00-5523-00 |
| Intracellular Fixation and Permeabilization Set | eBioscience | Cat# 88-8824-00 |
| Ionomycin calcium salt from Streptomyces | Sigma | Cat# I0634-1MG |
| L-glutamine 200mM | GIBCO | Cat# 25030-081 |
| Liberase™ DL Research Grade | Sigma | Cat# 5401160001 |
| Liberase™ TL Research | Sigma | Cat# 5466202001 |
| Non-essential amino acids | GIBCO | Cat# 11140-035 |
| PBS | GIBCO | Cat# 20012-068 |
| Percoll® | Sigma | Cat# P1644-100ML |
| PMA (Phorbol 12-myristate 13-acetate) | Sigma | Cat# P8139-1MG |
| RBC Lysis Buffer | eBioscience | Cat# 00-4300-54 |
| RPMI 1640 | GIBCO | Cat# 21875034 |
| UltraComp eBeads Plus Compensation Beads | Invitrogen | Cat# 01-3333-42 |
| Zombie Aqua™ Viability Stain | Biolegend | Cat# 423101 |
| | | |
| Deposited Data | | |
| Single cell RNA/TCRseq data of T cells from CT2A tumor | This paper | GEO: *in progress, raw and processed data files available upon request* |
| Single cell RNAseq of CD45 cells from CT2A tumor | (Tomaszewski et al. 2022) | GEO: GSE197879 |
| Single cell RNAseq from human newly diagnosed GBM | (Abdelfattah et al., 2022) | GEO: GSE160189 |
| Single cell RNAseq from human metastatic brain melanoma | (Biermann et al., 2022) | GEO: GSE200218 |

| | | |
|---|---|---|
| Experimental Models: Cell lines | | |
| CT2A | Massachusetts General Hospital | (Martinez-Murillo et al., 2007) |
| CT2A-TRP2 | Duke University | N/A |
| CT2A-TRP2-β2mKO | Duke University | N/A |
| CT2A-TRP2-OVA | Duke University | N/A |
| CT2A-GFP-LUC | Duke University | (Swan et al., 2023) |
| B16F0 | ATCC | CRL-6322 |
| LLC | ATCC | CRL-1642 |
| E0771 | ATCC | CRL-3461 |
| | | |
| Experimental Models: Organisms/Strains | | |
| Mouse: C57BL/6J | Jackson | Strain# 000664; RRID: IMSR_JAX:000664 |
| Mouse: B6.SJL-Ptprc$^{a}$ Pepc$^{b}$/BoyJ | Jackson | Strain# 002014; RRID: IMSR_JAX:002014 |
| Mouse: B6.129S4-Ccr2tm1Ifc/J | Jackson | Strain# 004999; RRID: IMSR_JAX:004999 |
| Mouse: B6.129P2-B2mtm1Unc/DcrJ | Jackson | Strain# 002087; RRID: IMSR_JAX:002087 |
| Mouse: B6.FVB-1700016L21RikTg(Itgax-DTR/EGFP)57Lan/J | Jackson | Strain# 004509; RRID: IMSR_JAX:004509 |
| Mouse: C57BL/6-Tg(TcraTcrb)1100Mjb/J | Jackson | Strain# 003831; RRID: IMSR_JAX:003831 |
| | | |
| Software and Algorithms | | |
| Flowjo | FlowJo, LLC | https://www.flowjo.com/ |
| R 3.6.1 | CRAN | https://cran.r-project.org/bin/macosx/ |
| RStudio 2022.07.1 | RStudio | https://posit.co/download/rstudio-desktop/ |
| Seurat V4.0.3 | (Stuart et al., 2019) | https://satijalab.org/seurat/ |
| CellChat | (Jin et al., 2021) | https://www.cellchat.org/ |
| CellRanger 4.0.0 | 10X Genomics | https://www.10xgenomics.com/ |
| scRepertoire | (Borcherding et al., 2020) | https://github.com/ncborcherding/scRepertoire |
| fgsea | (Korotkevich et al., 2021) | https://github.com/ctlab/fgsea |

| | | |
|---|---|---|
| FIJI (v.2.13.1) | ImageJ | https://imagej.net/software/fiji/; RRID:SCR_002285 |
| | | |
| Other Resources | | |
| 70 μM cell strainers | Corning Falcon | Cat# 352350 |
| Dounce Tissue Grinders, Wheaton | VWR | Cat# 62400-620 |
| | | |

# RESOURCE AVAILABILITY

## Lead contact

Further information and requests should be directed to Peter Fecci.

## Materials availability

Materials generated by this study are available upon request.

## Data and code availability

Raw FASTQ files and associated single cell RNA and TCR sequencing processed files have been uploaded to the NCBI Gene Expression Omnibus (GEO) database and are awaiting an accession number (raw and processed data files are available upon request). Custom R scripts for TCR, and RNA analysis are also available upon request.

# EXPERIMENTAL MODEL AND SUBJECT DETAILS

## Mice

All mice were used in accordance with National Institutes of Health and the Duke University Institutional Animal Care and Use Committee guidelines. C57BL/6J (cat #: 664), CCR2KO (cat #: 4999), CD11c-DTR (cat #: 4509), CD45.1 (cat #: 2014), and β2mKO (cat #: 2087) were purchased from Jackson Laboratory at 7-8 weeks.

## Tumor cell lines

C57BL/6 syngeneic CT2A glioma was provided by Robert L. Martuza (Massachusetts General Hospital)[45]. B16F0 melanoma, E0771 breast cancer, and Lewis lung cancer (LLC) were purchased from ATCC. CT2A-TRP2 was generated by overexpressing a TRP2-containing lentiviral plasmid. CT2A-TRP2-OVA was generated through lentiviral

584 transduction of parental CT2A-TRP2 with an OVA-containing lentiviral plasmid. CT2A-
585 GFP-LUC was kindly provided by Alexa Bramall and Nalini Mehta (Duke University)[46].
586 CT2A-TRP2-β2mKO was made through β2m knockout via CRISPR/Cas9. sgRNA
587 targeting murine β2m (gRNA sequence: AGUCGUCAGCAUGGCUCGCU) and Cas9
588 nuclease were purchased from STEMCELL technologies (Cat#: 200-0013, 76002,
589 respectively). sgRNA (5.8 µg) was incubated at room temperature with 10.8 µg Cas9
590 protein (STEMCELL Technologies, Cat#: 76002) in Opti-MEM™ + GlutaMAX™
591 (ThermoFisher Scientific Cat#: 51985034) for 20 min prior to electroporation.
592 sgRNA/Cas9 was then added to 2.5 x $10^5$ CT2A-Trp2 cells in Opti-MEM™ + GlutaMAX™.
593 Cells were electroporated in a 0.2 cm cuvette using a BioRad Gene Pulser XCell™ in
594 100ul total volume (exponential decay, 1000 uF, 155 V). Cells were FACS isolated after
595 96 h on H-2$K^b$/H-2$D^b$ negative cells. CT2A-TRP2-β2MKO cell line was established from
596 a single cell clone, cultured as described below. CT2A, CT2A-TRP2, CT2A-TRP2-OVA,
597 CT2A-TRP2- β2mKO, CT2A-GFP, E0771, LLC were cultured in complete DMEM (Gibco
598 11995-065, 10% FBS). B16F0 was cultured in complete DMEM + 1mM L-glutamine. All
599 cell lines were authenticated and tested negative for mycoplasma, and interspecies
600 contamination by IDEXX Laboratories.

601 # METHOD DETAILS

602 **Tumor cell line preparation and injection**

603 All cell lines were cultured at 37˚C in 5% $CO_2$, in their respective media. For tumor
604 inoculation, all cell lines were taken out of culture using 0.05% Trypsin, washed once with
605 media and once with PBS. Cells were resuspended in PBS for subcutaneous injections
606 (200 µl injection volume) and a 1:1 mix of PBS and methylcellulose for intracranial
607 injections (5 µl injection volume). $1\times10^4$ CT2A, $5\times10^4$ CT2A-TRP2, $5\times10^4$ CT2A-TRP2-
608 β2mKO, $5\times10^4$ CT2A-TRP2-OVA, $2.5\times10^4$ CT2A-GFP-LUC, $1\times10^3$ B16F0, $1\times10^3$
609 E0771, and $1\times10^3$ LLC were injected intracranially. $5\times10^5$ CT2A, $2.5\times10^5$ E0771, $1\times10^5$
610 B16F0 were injected subcutaneously. Mice were monitored and sacrificed in accordance
611 with Duke University Institutional Animal Care and Use Committee guidelines.

612

613 **In vivo antibody administration (aCD8, aCSF1R)**

614 For macrophage depletion experiments, 400µg aCSF1R (AFS98, BioXCell) was
615 administered 3 times weekly starting 2 days before tumor implantation into CCR2KO
616 mice, as described previously[33].

617 For $CD8^+$ T cell depletion, mice received 200ug anti-CD8$\alpha$ (clone 2.43; BioXCell) daily
618 for 3 days prior to tumor implantation, then every 5 days.

619

620 **Dendritic cell depletion**

621 CD11c-DTR or control C57Bl/6J mice were injected intraperitoneally with 5ng/g diptheria
622 toxin (Sigma-Aldrich, D0643) every 3 days, starting D8 after tumor implantation for 4
623 treatments as previously described[2].

624

625 **Microglia depletion**

626 C57Bl/6J mice were put on PLX3397 diet (290 mg/kg) or a control diet formulated in AIN-
627 76A standard chow as previously described[47].

628

629 **Mouse brain tumor tissue processing**

630 For processing intracranial tumors, brains were harvested as before[29]. In brief, mice were
631 transcardially perfused with 10ml PBS + 1% heparin. The tumor-bearing hemisphere was
632 mechanically dissociated with a dounce tissure homgenizer, then enzymatically
633 dissociated (0.05mg $ml^{-1}$ Liberase DL (Roche), 0.05 mg $ml^{-1}$ Liberase TL (Roche), 0.2 mg
634 $ml^{-1}$ Dnase I (Roche) in HBSS with $Ca^{2+}$ and $Mg^{2+}$) for 15 min at 37 ˚C. The single cell
635 suspension was then washed with PBS and resuspended in RBC lysis buffer (Invitrogen)
636 for 3 min. After quenching the lysis reaction with PBS, the cell suspension was passed
637 through a 70 µm filter. Myelin was removed from the sample with Percoll density gradient
638 centrifugation. Samples were resuspended in 30% Percoll (Sigma-Aldrich) and
639 centrifuged at 500 g for 20 min at 18 ˚C with low brake. The myelin layer was aspirated,
640 and cells were washed with PBS and counted for subsequent flow cytometry staining.

641

642 **Flow cytometry**

643 For cytokine re-stimulation, samples were resuspended in RPMI + 10% FBS at 0.5 - 1 ×
644 $10^7$ cells/ml in a 48 well plate after being counted. PMA (50 ng/ml) + Ionomycin (1000
645 ng/ml) + GolgiStop™ (BD Biosciences) + GolgiPlug™ (BD Biosciences) were added and
646 then samples were incubated for 4 h at 37 ˚C.

647 If no re-stimulation was necessary, samples were resuspended at 1-2 × $10^7$ cells/ml in
648 100µl PBS and transferred to a 96-well plate. Cells were resuspended in Zombie Aqua
649 Viability Dye (1:500, Biolegend) and incubated for 25 min at RT.

650 For extracellular staining, samples were resuspended in 50 µl TruStain FcX Plus (1:500,
651 Biolegend) in FACS (PBS + 2% FBS) for 15 min at RT. After blocking, 50 µl of a 2X
652 antibody mastermix were added and samples were incubated for 25 min at 4 ˚C. Stained
653 samples were washed with FACS, then fixed with 2% formaldehyde in PBS for 20 min at
654 4 ˚C.

655 For intracellular staining, cells were instead fixed and permeabilized with a 1X FoxP3
656 Fixation/Perm buffer (eBioscience FoxP3/Transcription Factor Staining Buffer Set,
657 Thermo Fisher Scientific) for 30 min at 4 ˚C. Intracellular antigens were stained for 30 min
658 in 1X perm buffer at RT.

659 Before sample acquisition, 10 µl of Count Bright counting beads (Thermo Fisher
660 Scientific) were added to each sample. Samples were acquired on an LSRII or Fortessa
661 (BD Biosciences) using FACS Diva software v.9 and analyzed using FlowJo v.10 (Tree
662 Star).

663

664 **Immunofluorescence**

665 Brains from PLX3397 treated tumor-bearing mice were harvested after intracardial
666 perfusion with 10ml 1% PFA and 10ml PBS. Brains were left in 1% PFA for 6 h, then
667 washed and placed in 10% sucrose for 48h. Once brains had sunk in the solution, they
668 were washed and snap frozen in tissue freezing media (General Data Company) then
669 kept at -80 ˚C. Frozen brains were sectioned at 25 µm and mounted onto slides. Sections

670 were rehydrated with PBS, then permeabilized with Triton-X and washed with PBS.
671 Permeabilzed sections were blocked using PBS and 2% BSA. Primary and secondary
672 antibodies were subsequently stained in PBS for 1 h at RT each. Slides were imaged on
673 a Leica STED confocal microscope (Leica). FIJI was used to process and analyze
674 images.

675

676 ***Ex vivo* TRP2-TCR transgenic T cell generation and adoptive transfer**

677 Spleens were harvested from CD45.1 mice. Spleens were processed through 70µm filters
678 then red blood cells were lysed with RBC lysis (Invitrogen). Splenocytes were plated at 2
679 $\times 10^6$ cells/ml in RPMI + 10% FBS, 50 U/ml IL-2, 2.5 µg/ml Concavalin A, L-glutamine
680 (Gibco), Pen/Strep (Gibco), 50 µM βME and kept in culture for 48h. Cells were then
681 retrovirally transduced with the pMX-TRP2- TCRβ-2A-α vector (a kind gift from Dr.
682 Schumacher, Netherlands Cancer Institute) as described previously[48]. This TCR
683 recognizes the $TRP2_{180-188}$ epitope in the context of $H\text{-}2K^b$. Briefly, HEK293T cells were
684 transfected with pCL-Eco and the TRP2 vector using Lipofectamine 2000 (Invitrogen).
685 Transduction was then performed in non-tissue culture treated 24-well plates, previously
686 coated with Retronectin (25 µg/ml) (Takara) by combining viral supernatant and activated
687 splenocytes and spinning for 1.5 h at 2000 RPM. Transgenic (Tg) TRP2-TCR T cells were
688 cultured for another 3 days before use, splitting daily. 10 X $10^6$ or 2.5 X $10^5$ Tg TRP2-
689 TCR T cells were adoptively transferred through tail vein or intracranial injection in 100 µl
690 PBS or 24 µl PBS, respectively.

691 OT1 T cells were isolated from OT1 mice by culturing OT1 splenocytes as above for 48
692 h.

693

694 **Chimera Generation**

695 Bone marrow was harvested from 7 week old donor mice (either C57BL/6J or β2mKO).
696 Recipient mice (CD45.1) received whole-body irradiation with a 9 Gy dose from a Cesium
697 irradiator (Mark I-68A $^{137}Cs$ irradiator, JL Shepherd and Associates). Recipient mice then
698 received an intravenous infusion of $10 \times 10^6$ donor bone marrow cells in 100 µl PBS.
699 Recipient mice were then put on antibiotic-treated water for 2 weeks post bone marrow

700 transfer.

701 After 10 weeks of reconstitution, chimerism was validated in the blood, with >95%
702 chimerism in all queried mice. Then, CT2A-TRP2 or CT2A-TRP2-β2mKO was implanted
703 intracranially into chimeras. On D7 post-implantation, $10 \times 10^6$ TRP2-TCR T cells were
704 adoptively transferred intravenously.

705

706 **scRNAseq library generation**

707 $CD3^+CD4^+$ or $CD3^+CD8^+$ were sorted from D13 (n = 16) and D19 (n = 4) intracranial
708 tumors. Four mice were pooled for each D13 replicate to achieve desired number of cells.
709 10,000 total cells from each timepoint were targeted with an average read depth of 36,000
710 reads per cell for the gene expression library. Reads were sequenced on a NovaSeq S1
711 flow cell. For the TCR library, 9,000 reads per cell were targeted and sequenced on a
712 NovaSeq SP.

713 *10x Transcriptome library prep:* GEMs are generated by combining barcoded Single Cell
714 5' Gel Beads, Master Mix, Partitioning Oil and single cells on a Chromium microfluidic
715 Chip. Immediately following GEM generation, the Gel Bead is dissolved and any co-
716 partitioned cell is lysed. Oligonucleotides containing an Illumina R1 sequence (read 1
717 sequencing primer), a 16 nt 10x Barcode, a 10 nt unique molecular identifier (UMI), and
718 13 nt template switch oligo (TSO) are released and mixed with the cell lysate and a Master
719 Mix containing reverse transcription (RT) reagents and poly(dT) RT primers. Incubation
720 of the GEMs produces 10x Barcoded, full-length cDNA from polyadenylated mRNA.

721 GEMs are then broken and pooled and the 10x Barcoded first-strand cDNA is purified
722 from the post GEM-RT reaction mixture and amplified. Full-length V(D)J segments (10x
723 Barcoded) are enriched from amplified cDNA via PCR amplification with universal primer
724 for 5' adapter and successive nested primers specific to the TCR and/or BCR constant
725 regions. Enrichment and library preparation of the TCR and BCR constant regions takes
726 place in two separate workflows using the same amplified cDNA stock.

727 Enzymatic fragmentation and size selection are used to generate variable length
728 fragments that collectively span the V(D)J segments of the enriched TCR and/or BCR

729 transcripts prior to library construction. P5, P7, a dual sample index, and an Illumina R2
730 sequence (read 2 primer sequence) are added via End Repair, A-tailing, Adaptor Ligation,
731 and Sample Index PCR. The final libraries contain the P5 and P7 priming sites used in
732 Illumina sequencing. Sequence is generated using Illumina short read paired end
733 sequencing.

734

735 **scRNAseq data processing and analysis**

736 The Cell Ranger pipeline (10X Genomics) was used to perform sample demultiplexing
737 and to generate FASTQ files for the gene expression and ADT libraries. FASTQ files were
738 demultiplexed from the raw sequencing reads (bcl2fastq, v2.20), aligned to the mouse
739 mm10 reference genome (cellranger, v4.0.0), and raw gene count matrices were
740 generated using STAR (v2.7.5c).

741 Downstream analysis was performed using the R software Seurat
742 package[49] (v4.0.3, http://satijalab.org/seurat/). Hashtag oligos, which corresponded to
743 biological replicates, were demultiplexed using the HTODemux function and appended to
744 the meta-data for each sample. Low-quality cells, expressing less than 200 genes, and
745 genes expressed by fewer than three cells were removed. The gene expression matrix
746 for each genotype was then concatenated using the merge function in Seurat. The
747 percentage of mitochondrial gene content was calculated using the
748 Mouse.MitoCarta3.0[50] gene set and the PercentageFeatureSet function in Seurat. The
749 Seurat object was converted to a SingleCellExperiment object, and outlier exclusion was
750 performed in scater (v.1.18.6). Using the isOutlier function in scater, cells were discarded
751 if their percentage of mitochondrial gene content, number of expressed genes, or number
752 of reads for a given cell was considered an outlier. A total of 6,742 $CD8^+$ cells passed QC
753 and the SingleCellExperiment object was then converted back into a Seurat object.
754 Normalization and regression of cell cycle scoring and percent mitochondrial gene
755 content were performed using the SCTransform function in Seurat. Principal component
756 analysis (PCA) was performed on all genes, and the number of principal components to
757 be utilized in further analysis was determined heuristically using the elbow method.
758 Eleven principal components were used for clustering and dimensionality reduction using

759 FindNeighbors, RunUMAP, and a resolution of 0.5 was used for FindClusters in Seurat.
760 This approach identified six distinct cell clusters. All subsequent analyses were conducted
761 with this cleaned object.

762 For TCRSeq analysis, scRepertoire standard workflow was utilized[51]. In brief filtered
763 contig outputs from the 10X Genomics Cell Ranger Pipeline were loaded into R (v4.1.2)
764 and combined into a list using combineTCR. Next combineExpression was used to attach
765 clonotypic information to the Seurat object. Visualizations were made using the
766 scRepertoire vignette.

767 For exhaustion signature score generation, the built in AddModuleScore function from
768 Seurat was utilized with a gene list from Im et al. 2016[19]. A detailed list can be found in
769 Table S1. For pseudotime analysis, the object was passed into Monocle v3 without any
770 changes to the UMAP dimensional reduction.

771

772 **Publicly available scRNA-seq data analysis**

773 Human newly diagnosed GBM and metastatic brain melanoma datasets were
774 downloaded from the GEO (accession # :GSE160189, GSE200218). Datasets were QC'd
775 as above, removing cells with high mitochondrial percentage and those that lacked
776 expression of PTPRC1 (non-immune cells). Then datasets were integrated using the
777 standard Seurat protocol[52].

778

779 **Cellchat Analysis Mouse/Human**

780 For murine CellChat analysis utilizing the CD45+ sorted dataset generated by
781 Tomaszewski et al[29], we subsetted the object to keep CD8 TIL, Apoe+ TAM, Nos2+ TAM,
782 DC1, DC2, DC3, pDC and microglia from the WT sample. We then fed this cleaned object
783 into the CellChat pipeline with built in murine ligand-receptor database. Following the
784 recommended vignette, we visualized the enrichment of the MHC-I pathway across cell
785 types. Additionaly we visualized the strength and number of interactions with CD8 TIL as
786 the target cells.

787 Human CellChat analysis followed a similar workflow, except the human ligand-receptor

788 database was utilized. Additionally, integrated ndGBM and MBM was subsetted so
789 samples of the same tumor type were analyzed separately, as suggested by the CellChat
790 vignette.

# 791 QUANTIFICATION AND STATISTICAL ANALYSIS

## 792 Statistical Analysis

793 Unless specifically noted, all data are representative of ≥2 separate experiments.
794 Experimental group assignment was determined by random designation. Statistical
795 analyses were performed using GraphPad Prism software. Error bars represent ±
796 Standard Error of the mean (SEM) calculated using Prism. Specific statistical tests used
797 were paired t-tests, unpaired t-tests, and one/two-way ANOVA unless otherwise noted.
798 P-values <0.05 were considered statistically significant. Investigators were not blinded to
799 group assignment during experimental procedures or analysis.

# 800 SUPPLEMENTAL INFORMATION TITLES AND METHODS

801 Supplemental Figure 1:

802 (A) Gating strategy for Tex_prog and Tex_term.

803 (B) Frequency of Tex subsets of PD1+CD44+ CD8+ T cells in intracranial B16F0, LLC or
804 CT2A. n = 8-10 mice/group.

805 All of the data are means ± SEMs; p-values are shown on individual plots as determined
806 by 1-way ANOVA and post-hoc Tukey test (B), two-sided paired t-test (B).

807

808 Supplemental Figure 2:

809 (A) Dot plot of top 3 genes for each cluster.

810 (B) Violin plot of *Tcf7, Pdcd1, Tox,* and *Havcr2* expression across clusters.

811 (C) UMAP of cloneType across biological replicates (n=4 per timepoint).

812 (D) Shannon and Inverse Simpson diversity indices across clusters, calculated with the
813 scRepertoire package.

814 (E) 10 most expanded TCR clones across timepoints are concentrated to Tex_int and
815 Tex_term clusters.

816

817 Supplemental Figure 3:

818 (A) PD1 expression on transferred OT1 vs. TRP2-TCR Tg T cells on day of ALT (D7) and
819 day of tumor harvest (D21) and representative histogram. n = 7 mice/group.

820 (B) Frequency of Tex subsets of PD1+ endogenous or transgenic TRP2-TCR T cells and
821 representative contour plot. n = 7 mice.

822 (C) gMFI of MHC I in CT2A-TRP2 vs. CT2A-TRP2-B2mKO validating knockout of MHC
823 I. n = 10 mice/group.

824 (D) Number of TRP2-TCR T cells/g of tumor in CT2A-TRP2 vs. CT2A-TRP2-B2mKO. n
825 = 10 mice/group.

826 p-values are plotted on individual graphs. Statistical significance was determined by two-
827 sided unpaired t-test (A, C, D) or 2-way RM ANOVA with post-hoc Tukey's test for multiple
828 comparisons (B). All data are plotted as mean ± SEM. See also Figure S4.

829

830 Supplemental Figure 4:

831 (A) Interaction strength across APC with CD8 TIL as the target.

832 (B) Gating strategy for intratumoral APC.

833

834 Supplemental Figure 5:

835 (A) Frequency of TAM of $CD45^+$ cells. Data pooled from 2 independent experiments. n =
836 11 mice/group.

837 (B) Experimental layout. DC were depleted in CD11c-DTR mice with 5ng/g DT, every 3
838 days for 4 total treatments, starting D8. Created with Biorender.com.

839 (C) Frequency of CD11c+CD11b- DC in WT vs. CD11c-DTR mice.

840 (D) Experimental layout. Microglia were depleted in WT mice with 270mg/kg PLX3397
841 chow. Chow was provided starting D(-)14. Created with Biorender.com.

842 (E) Representative immunofluorescence image of WT vs. PLX3397 treated non-tumor
843 brain. Scale bar = 100um.

844 (F) Chimera validation. Frequency of MHC I+ in WT → WT (WT) or B2mKO → WT
845 (B2mKO) chimeras across T cells, TAM and cDC. n = 8-10 mice/group.

846 (G) Representative histogram of MHC I expression on TAM in the setting of CT2A-TRP2
847 (Teal) vs. CT2A-TRP2-B2mKO (Dark Teal).

848 (H) Frequency of TAM of $CD45^+$ cells in B16F0 IC. n = 9-10 mice/group.

849 (I) Frequency of TAM of $CD45^+$ cells in B16F0 SQ. Data pooled from 2 independent
850 experiments. n = 6-7 mice/group.

851 p-values are plotted on individual graphs. Statistical significance was determined by two-
852 sided unpaired t test (A, H, I) or RM-2-way ANOVA with post-hoc Tukey's test for multiple
853 comparisons (F). All data are plotted as mean ± SEM.

854 References:


855 1. Nolan, C., and Deangelis, L.M. (2018). Overview of metastatic disease of the central
856 nervous system. Handb Clin Neurol *149*, 3-23. 10.1016/B978-0-12-811161-1.00001-3.
857 2. Jung, S., Unutmaz, D., Wong, P., Sano, G., De los Santos, K., Sparwasser, T., Wu, S.,
858 Vuthoori, S., Ko, K., Zavala, F., et al. (2002). In vivo depletion of CD11c+ dendritic cells
859 abrogates priming of CD8+ T cells by exogenous cell-associated antigens. Immunity *17*,
860 211-220. 10.1016/s1074-7613(02)00365-5.
861 3. Amin, S., Baine, M.J., Meza, J.L., and Lin, C. (2020). Association of Immunotherapy With
862 Survival Among Patients With Brain Metastases Whose Cancer Was Managed With
863 Definitive Surgery of the Primary Tumor. JAMA Netw Open *3*, e2015444.
864 10.1001/jamanetworkopen.2020.15444.
865 4. Brastianos, P.K., Curry, W.T., and Oh, K.S. (2013). Clinical discussion and review of the
866 management of brain metastases. J Natl Compr Canc Netw *11*, 1153-1164.
867 10.6004/jnccn.2013.0133.
868 5. Reardon, D.A., Brandes, A.A., Omuro, A., Mulholland, P., Lim, M., Wick, A., Baehring, J.,
869 Ahluwalia, M.S., Roth, P., Bahr, O., et al. (2020). Effect of Nivolumab vs Bevacizumab in
870 Patients With Recurrent Glioblastoma: The CheckMate 143 Phase 3 Randomized Clinical
871 Trial. JAMA Oncol *6*, 1003-1010. 10.1001/jamaoncol.2020.1024.
872 6. Woroniecka, K., Chongsathidkiet, P., Rhodin, K., Kemeny, H., Dechant, C., Farber, S.H.,
873 Elsamadicy, A.A., Cui, X., Koyama, S., Jackson, C., et al. (2018). T-Cell Exhaustion Signatures
874 Vary with Tumor Type and Are Severe in Glioblastoma. Clin Cancer Res *24*, 4175-4186.
875 10.1158/1078-0432.CCR-17-1846.
876 7. Woroniecka, K.I., Rhodin, K.E., Chongsathidkiet, P., Keith, K.A., and Fecci, P.E. (2018). T-
877 cell Dysfunction in Glioblastoma: Applying a New Framework. Clin Cancer Res *24*, 3792-
878 3802. 10.1158/1078-0432.ccr-18-0047.
879 8. Akbay, E.A., Koyama, S., Carretero, J., Altabef, A., Tchaicha, J.H., Christensen, C.L., Mikse,
880 O.R., Cherniack, A.D., Beauchamp, E.M., Pugh, T.J., et al. (2013). Activation of the PD-1
881 pathway contributes to immune escape in EGFR-driven lung tumors. Cancer discovery *3*,
882 1355-1363. 10.1158/2159-8290.CD-13-0310.
883 9. Koyama, S., Akbay, E.A., Li, Y.Y., Herter-Sprie, G.S., Buczkowski, K.A., Richards, W.G.,
884 Gandhi, L., Redig, A.J., Rodig, S.J., Asahina, H., et al. (2016). Adaptive resistance to
885 therapeutic PD-1 blockade is associated with upregulation of alternative immune
886 checkpoints. Nat Commun *7*, 10501. 10.1038/ncomms10501.
887 10. Huang, R.Y., Francois, A., McGray, A.R., Miliotto, A., and Odunsi, K. (2017). Compensatory
888 upregulation of PD-1, LAG-3, and CTLA-4 limits the efficacy of single-agent checkpoint
889 blockade in metastatic ovarian cancer. Oncoimmunology *6*, e1249561.
890 10.1080/2162402X.2016.1249561.
891 11. Shayan, G., Srivastava, R., Li, J., Schmitt, N., Kane, L.P., and Ferris, R.L. (2017). Adaptive
892 resistance to anti-PD1 therapy by Tim-3 upregulation is mediated by the PI3K-Akt
893 pathway in head and neck cancer. Oncoimmunology *6*, e1261779.
894 10.1080/2162402X.2016.1261779.
895 12. Thommen, D.S., Schreiner, J., Muller, P., Herzig, P., Roller, A., Belousov, A., Umana, P.,
896 Pisa, P., Klein, C., Bacac, M., et al. (2015). Progression of Lung Cancer Is Associated with

897 Increased Dysfunction of T Cells Defined by Coexpression of Multiple Inhibitory
898 Receptors. Cancer Immunol Res *3*, 1344-1355. 10.1158/2326-6066.CIR-15-0097.
899 13. Dunn, G.P., Fecci, P.E., and Curry, W.T. (2012). Cancer immunoediting in malignant
900 glioma. Neurosurgery *71*, 201-222; discussion 222-203.
901 10.1227/NEU.0b013e31824f840d.
902 14. Wherry, E.J., Ha, S.J., Kaech, S.M., Haining, W.N., Sarkar, S., Kalia, V., Subramaniam, S.,
903 Blattman, J.N., Barber, D.L., and Ahmed, R. (2007). Molecular signature of CD8+ T cell
904 exhaustion during chronic viral infection. Immunity *27*, 670-684.
905 10.1016/j.immuni.2007.09.006.
906 15. Kallies, A., Zehn, D., and Utzschneider, D.T. (2020). Precursor exhausted T cells: key to
907 successful immunotherapy? Nat Rev Immunol *20*, 128-136. 10.1038/s41577-019-0223-7.
908 16. Utzschneider, D.T., Gabriel, S.S., Chisanga, D., Gloury, R., Gubser, P.M., Vasanthakumar,
909 A., Shi, W., and Kallies, A. (2020). Early precursor T cells establish and propagate T cell
910 exhaustion in chronic infection. Nat Immunol *21*, 1256-1266. 10.1038/s41590-020-0760-
911 z.
912 17. Angelosanto, J.M., Blackburn, S.D., Crawford, A., and Wherry, E.J. (2012). Progressive loss
913 of memory T cell potential and commitment to exhaustion during chronic viral infection.
914 J Virol *86*, 8161-8170. 10.1128/JVI.00889-12.
915 18. Woroniecka, K., Chongsathidkiet, P., Rhodin, K.E., Kemeny, H.R., Dechant, C.A., Farber,
916 S.H., Elsamadicy, A.A., Cui, X., Koyama, S., Jackson, C.C., et al. (2018). T Cell Exhaustion
917 Signatures Vary with Tumor Type and are Severe in Glioblastoma. Clin Cancer Res.
918 10.1158/1078-0432.ccr-17-1846.
919 19. Im, S.J., Hashimoto, M., Gerner, M.Y., Lee, J., Kissick, H.T., Burger, M.C., Shan, Q., Hale,
920 J.S., Lee, J., Nasti, T.H., et al. (2016). Defining CD8+ T cells that provide the proliferative
921 burst after PD-1 therapy. Nature *537*, 417-421. 10.1038/nature19330.
922 20. Utzschneider, D.T., Charmoy, M., Chennupati, V., Pousse, L., Ferreira, D.P., Calderon-
923 Copete, S., Danilo, M., Alfei, F., Hofmann, M., Wieland, D., et al. (2016). T Cell Factor 1-
924 Expressing Memory-like CD8(+) T Cells Sustain the Immune Response to Chronic Viral
925 Infections. Immunity *45*, 415-427. 10.1016/j.immuni.2016.07.021.
926 21. Miller, B.C., Sen, D.R., Al Abosy, R., Bi, K., Virkud, Y.V., LaFleur, M.W., Yates, K.B., Lako, A.,
927 Felt, K., Naik, G.S., et al. (2019). Author Correction: Subsets of exhausted CD8(+) T cells
928 differentially mediate tumor control and respond to checkpoint blockade. Nat Immunol
929 *20*, 1556. 10.1038/s41590-019-0528-5.
930 22. Sade-Feldman, M., Yizhak, K., Bjorgaard, S.L., Ray, J.P., de Boer, C.G., Jenkins, R.W., Lieb,
931 D.J., Chen, J.H., Frederick, D.T., Barzily-Rokni, M., et al. (2018). Defining T Cell States
932 Associated with Response to Checkpoint Immunotherapy in Melanoma. Cell *175*, 998-
933 1013 e1020. 10.1016/j.cell.2018.10.038.
934 23. Schietinger, A., Philip, M., Krisnawan, V.E., Chiu, E.Y., Delrow, J.J., Basom, R.S., Lauer, P.,
935 Brockstedt, D.G., Knoblaugh, S.E., Hammerling, G.J., et al. (2016). Tumor-Specific T Cell
936 Dysfunction Is a Dynamic Antigen-Driven Differentiation Program Initiated Early during
937 Tumorigenesis. Immunity *45*, 389-401. 10.1016/j.immuni.2016.07.011.
938 24. McLane, L.M., Abdel-Hakeem, M.S., and Wherry, E.J. (2019). CD8 T Cell Exhaustion During
939 Chronic Viral Infection and Cancer. Annu Rev Immunol *37*, 457-495. 10.1146/annurev-
940 immunol-041015-055318.

941 25. Connolly, K.A., Kuchroo, M., Venkat, A., Khatun, A., Wang, J., William, I., Hornick, N.I.,
942 Fitzgerald, B.L., Damo, M., Kasmani, M.Y., et al. (2021). A reservoir of stem-like CD8(+) T
943 cells in the tumor-draining lymph node preserves the ongoing antitumor immune
944 response. Sci Immunol *6*, eabg7836. 10.1126/sciimmunol.abg7836.
945 26. Prokhnevska, N., Cardenas, M.A., Valanparambil, R.M., Sobierajska, E., Barwick, B.G.,
946 Jansen, C., Reyes Moon, A., Gregorova, P., delBalzo, L., Greenwald, R., et al. (2023). CD8(+)
947 T cell activation in cancer comprises an initial activation phase in lymph nodes followed
948 by effector differentiation within the tumor. Immunity *56*, 107-124 e105.
949 10.1016/j.immuni.2022.12.002.
950 27. Postow, M.A., Manuel, M., Wong, P., Yuan, J., Dong, Z., Liu, C., Perez, S., Tanneau, I., Noel,
951 M., Courtier, A., et al. (2015). Peripheral T cell receptor diversity is associated with clinical
952 outcomes following ipilimumab treatment in metastatic melanoma. J Immunother Cancer
953 *3*, 23. 10.1186/s40425-015-0070-4.
954 28. Klemm, F., Maas, R.R., Bowman, R.L., Kornete, M., Soukup, K., Nassiri, S., Brouland, J.P.,
955 Iacobuzio-Donahue, C.A., Brennan, C., Tabar, V., et al. (2020). Interrogation of the
956 Microenvironmental Landscape in Brain Tumors Reveals Disease-Specific Alterations of
957 Immune Cells. Cell *181*, 1643-1660 e1617. 10.1016/j.cell.2020.05.007.
958 29. Tomaszewski, W.H., Waibl-Polania, J., Chakraborty, M., Perera, J., Ratiu, J., Miggelbrink,
959 A., McDonnell, D.P., Khasraw, M., Ashley, D.M., Fecci, P.E., et al. (2022). Neuronal CaMKK2
960 promotes immunosuppression and checkpoint blockade resistance in glioblastoma. Nat
961 Commun *13*, 6483. 10.1038/s41467-022-34175-y.
962 30. Jin, S., Guerrero-Juarez, C.F., Zhang, L., Chang, I., Ramos, R., Kuan, C.H., Myung, P., Plikus,
963 M.V., and Nie, Q. (2021). Inference and analysis of cell-cell communication using CellChat.
964 Nat Commun *12*, 1088. 10.1038/s41467-021-21246-9.
965 31. Joffre, O.P., Segura, E., Savina, A., and Amigorena, S. (2012). Cross-presentation by
966 dendritic cells. Nat Rev Immunol *12*, 557-569. 10.1038/nri3254.
967 32. Boring, L., Gosling, J., Chensue, S.W., Kunkel, S.L., Farese, R.V., Jr., Broxmeyer, H.E., and
968 Charo, I.F. (1997). Impaired monocyte migration and reduced type 1 (Th1) cytokine
969 responses in C-C chemokine receptor 2 knockout mice. J Clin Invest *100*, 2552-2561.
970 10.1172/JCI119798.
971 33. MacDonald, K.P., Palmer, J.S., Cronau, S., Seppanen, E., Olver, S., Raffelt, N.C., Kuns, R.,
972 Pettit, A.R., Clouston, A., Wainwright, B., et al. (2010). An antibody against the colony-
973 stimulating factor 1 receptor depletes the resident subset of monocytes and tissue- and
974 tumor-associated macrophages but does not inhibit inflammation. Blood *116*, 3955-3963.
975 10.1182/blood-2010-02-266296.
976 34. Miyake, K., and Karasuyama, H. (2021). The Role of Trogocytosis in the Modulation of
977 Immune Cell Functions. Cells *10*. 10.3390/cells10051255.
978 35. Abdelfattah, N., Kumar, P., Wang, C., Leu, J.S., Flynn, W.F., Gao, R., Baskin, D.S.,
979 Pichumani, K., Ijare, O.B., Wood, S.L., et al. (2022). Single-cell analysis of human glioma
980 and immune cells identifies S100A4 as an immunotherapy target. Nat Commun *13*, 767.
981 10.1038/s41467-022-28372-y.
982 36. Biermann, J., Melms, J.C., Amin, A.D., Wang, Y., Caprio, L.A., Karz, A., Tagore, S., Barrera,
983 I., Ibarra-Arellano, M.A., Andreatta, M., et al. (2022). Dissecting the treatment-naive

984 ecosystem of human melanoma brain metastasis. Cell *185*, 2591-2608 e2530.
985 10.1016/j.cell.2022.06.007.
986 37. Salmon, H., Remark, R., Gnjatic, S., and Merad, M. (2019). Host tissue determinants of
987 tumour immunity. Nat Rev Cancer *19*, 215-227. 10.1038/s41568-019-0125-9.
988 38. Karimi, E., Yu, M.W., Maritan, S.M., Perus, L.J.M., Rezanejad, M., Sorin, M., Dankner, M.,
989 Fallah, P., Dore, S., Zuo, D., et al. (2023). Single-cell spatial immune landscapes of primary
990 and metastatic brain tumours. Nature *614*, 555-563. 10.1038/s41586-022-05680-3.
991 39. Jansen, C.S., Prokhnevska, N., Master, V.A., Sanda, M.G., Carlisle, J.W., Bilen, M.A.,
992 Cardenas, M., Wilkinson, S., Lake, R., Sowalsky, A.G., et al. (2019). An intra-tumoral niche
993 maintains and differentiates stem-like CD8 T cells. Nature *576*, 465-470. 10.1038/s41586-
994 019-1836-5.
995 40. Blackburn, S.D., Shin, H., Haining, W.N., Zou, T., Workman, C.J., Polley, A., Betts, M.R.,
996 Freeman, G.J., Vignali, D.A., and Wherry, E.J. (2009). Coregulation of CD8+ T cell
997 exhaustion by multiple inhibitory receptors during chronic viral infection. Nat Immunol
998 *10*, 29-37. 10.1038/ni.1679.
999 41. Engelhardt, J.J., Boldajipour, B., Beemiller, P., Pandurangi, P., Sorensen, C., Werb, Z.,
1000 Egeblad, M., and Krummel, M.F. (2012). Marginating dendritic cells of the tumor
1001 microenvironment cross-present tumor antigens and stably engage tumor-specific T cells.
1002 Cancer Cell *21*, 402-417. 10.1016/j.ccr.2012.01.008.
1003 42. Broz, M.L., Binnewies, M., Boldajipour, B., Nelson, A.E., Pollack, J.L., Erle, D.J., Barczak, A.,
1004 Rosenblum, M.D., Daud, A., Barber, D.L., et al. (2014). Dissecting the Tumor Myeloid
1005 Compartment Reveals Rare Activating Antigen-Presenting Cells Critical for T Cell
1006 Immunity. Cancer Cell *26*, 938. 10.1016/j.ccell.2014.11.010.
1007 43. Kersten, K., Hu, K.H., Combes, A.J., Samad, B., Harwin, T., Ray, A., Rao, A.A., Cai, E.,
1008 Marchuk, K., Artichoker, J., et al. (2022). Spatiotemporal co-dependency between
1009 macrophages and exhausted CD8(+) T cells in cancer. Cancer Cell *40*, 624-638 e629.
1010 10.1016/j.ccell.2022.05.004.
1011 44. Kilian, M., Sheinin, R., Tan, C.L., Friedrich, M., Kramer, C., Kaminitz, A., Sanghvi, K., Lindner,
1012 K., Chih, Y.C., Cichon, F., et al. (2023). MHC class II-restricted antigen presentation is
1013 required to prevent dysfunction of cytotoxic T cells by blood-borne myeloids in brain
1014 tumors. Cancer Cell *41*, 235-251 e239. 10.1016/j.ccell.2022.12.007.
1015 45. Martinez-Murillo, R., and Martinez, A. (2007). Standardization of an orthotopic mouse
1016 brain tumor model following transplantation of CT-2A astrocytoma cells. Histol
1017 Histopathol *22*, 1309-1326. 10.14670/HH-22.1309.
1018 46. Swan, S.L., Mehta, N., Ilich, E., Shen, S.H., Wilkinson, D.S., Anderson, A.R., Segura, T.,
1019 Sanchez-Perez, L., Sampson, J.H., and Bellamkonda, R.V. (2023). IL7 and IL7 Flt3L co-
1020 expressing CAR T cells improve therapeutic efficacy in mouse EGFRvIII heterogeneous
1021 glioblastoma. Front Immunol *14*, 1085547. 10.3389/fimmu.2023.1085547.
1022 47. Elmore, M.R., Najafi, A.R., Koike, M.A., Dagher, N.N., Spangenberg, E.E., Rice, R.A.,
1023 Kitazawa, M., Matusow, B., Nguyen, H., West, B.L., and Green, K.N. (2014). Colony-
1024 stimulating factor 1 receptor signaling is necessary for microglia viability, unmasking a
1025 microglia progenitor cell in the adult brain. Neuron *82*, 380-397.
1026 10.1016/j.neuron.2014.02.040.

1027 48. Bendle, G.M., Linnemann, C., Hooijkaas, A.I., Bies, L., de Witte, M.A., Jorritsma, A., Kaiser,
1028 A.D., Pouw, N., Debets, R., Kieback, E., et al. (2010). Lethal graft-versus-host disease in
1029 mouse models of T cell receptor gene therapy. Nat Med *16*, 565-570, 561p following 570.
1030 10.1038/nm.2128.
1031 49. Butler, A., Hoffman, P., Smibert, P., Papalexi, E., and Satija, R. (2018). Integrating single-
1032 cell transcriptomic data across different conditions, technologies, and species. Nat
1033 Biotechnol *36*, 411-420. 10.1038/nbt.4096.
1034 50. Rath, S., Sharma, R., Gupta, R., Ast, T., Chan, C., Durham, T.J., Goodman, R.P., Grabarek,
1035 Z., Haas, M.E., Hung, W.H.W., et al. (2021). MitoCarta3.0: an updated mitochondrial
1036 proteome now with sub-organelle localization and pathway annotations. Nucleic Acids
1037 Res *49*, D1541-D1547. 10.1093/nar/gkaa1011.
1038 51. Borcherding, N., Bormann, N.L., and Kraus, G. (2020). scRepertoire: An R-based toolkit for
1039 single-cell immune receptor analysis. F1000Res *9*, 47. 10.12688/f1000research.22139.2.
1040 52. Stuart, T., Butler, A., Hoffman, P., Hafemeister, C., Papalexi, E., Mauck, W.M., 3rd, Hao,
1041 Y., Stoeckius, M., Smibert, P., and Satija, R. (2019). Comprehensive Integration of Single-
1042 Cell Data. Cell *177*, 1888-1902 e1821. 10.1016/j.cell.2019.05.031.

1043

# Main Figures:

## Antigen-presentation by tumor-associated macrophages mediates progenitor to terminal exhaustion transition in GBM and other solid tumors

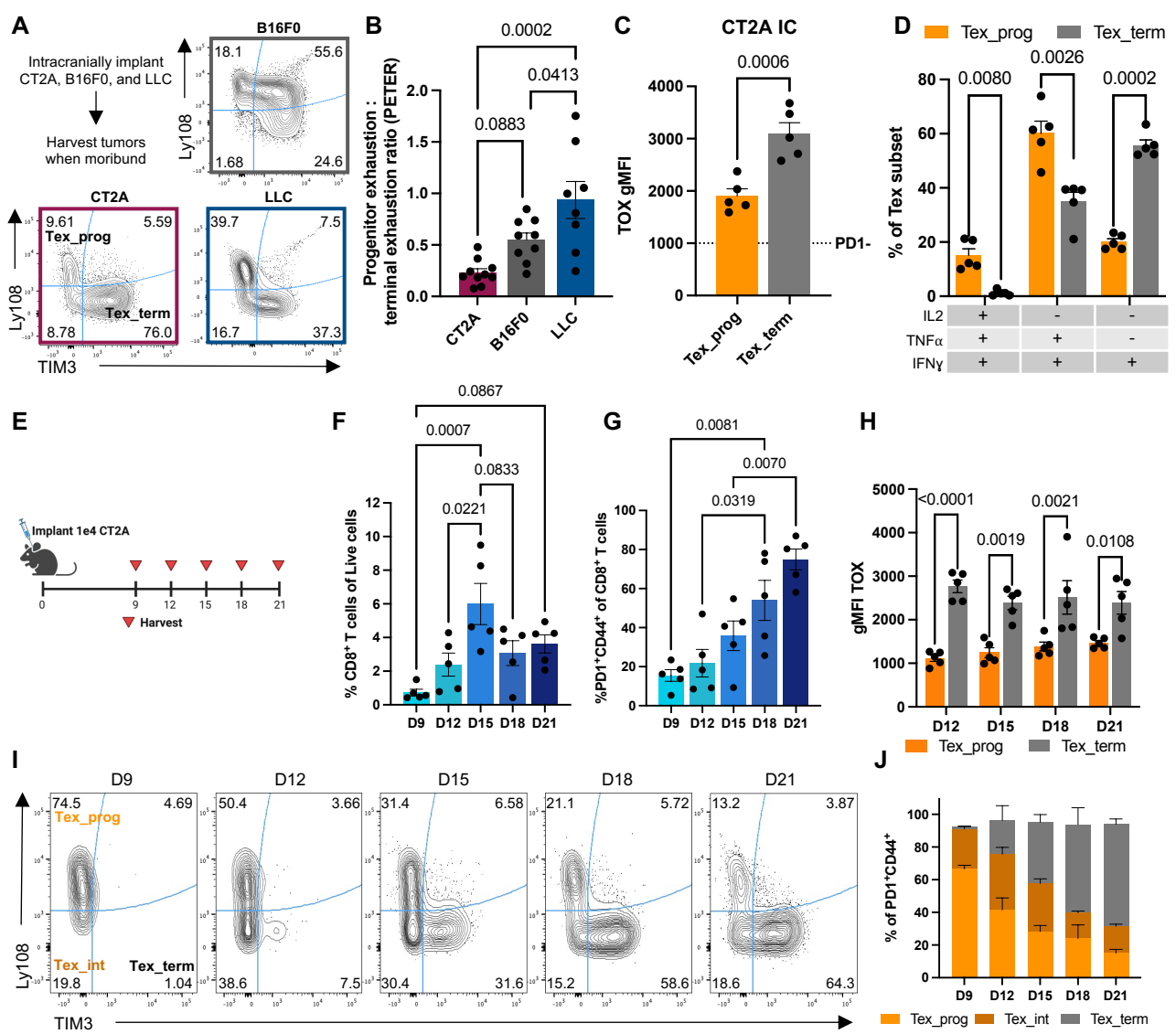


**Figure 1: GBM TIL demonstrate a severe decline in the Progenitor Exhaustion to Terminal Exhaustion (PETE) Ratio over time**

(A) Representative contour plots of Tex_prog and Tex_term across tumor types.

(B) PETER across CT2A, B16F0 and LLC intracranial tumors, harvested when mice were moribund. n = 8-10 mice/group.

(C and D) Geometric mean fluorescence intensity (gMFI) of intracellular TOX expression (C) and quantification of TNFa/IFNy/IL2 of Tex_prog and Tex_term in 10K CT2A at D18 (D). n = 5 mice. Representative of two independent experiments.

(E) Experimental layout. 10K CT2A cells implanted D0, tumors were harvested every 3 days starting D9 until mice were moribund on D21. Created with Biorender.

(F) number of CD8+ T cells per harvested tumor. n = 5 mice/timepoint.

(G) Frequency of PD1$^+$CD44$^+$ of CD8$^+$ T cells. n = 5 mice/timepoint

(H) Geometric mean fluorescence intensity (gMFI) of TOX of Tex_prog and Tex_term across timepoints with >100 total PD1$^+$CD44$^+$ CD8$^+$ T cells. n = 5 mice/timepoint

(I and J) Representative plots showing Ly108 vs. TIM3 progression from D9 to D21, Tex_prog = top left, Tex_int = bottom left, Tex_term = bottom right (I) and quantification of Tex subsets of PD1+CD44+ CD8+ T cells over time (J). n = 5 mice/timepoint

All of the data are means ± SEMs; p-values are shown on individual plots as determined by 1-way ANOVA and post-hoc Tukey test (B. F. G), two-sided paired t-test (C) or RM 2-way ANOVA and post-hoc Tukey test (D and H). See also Figure S1.

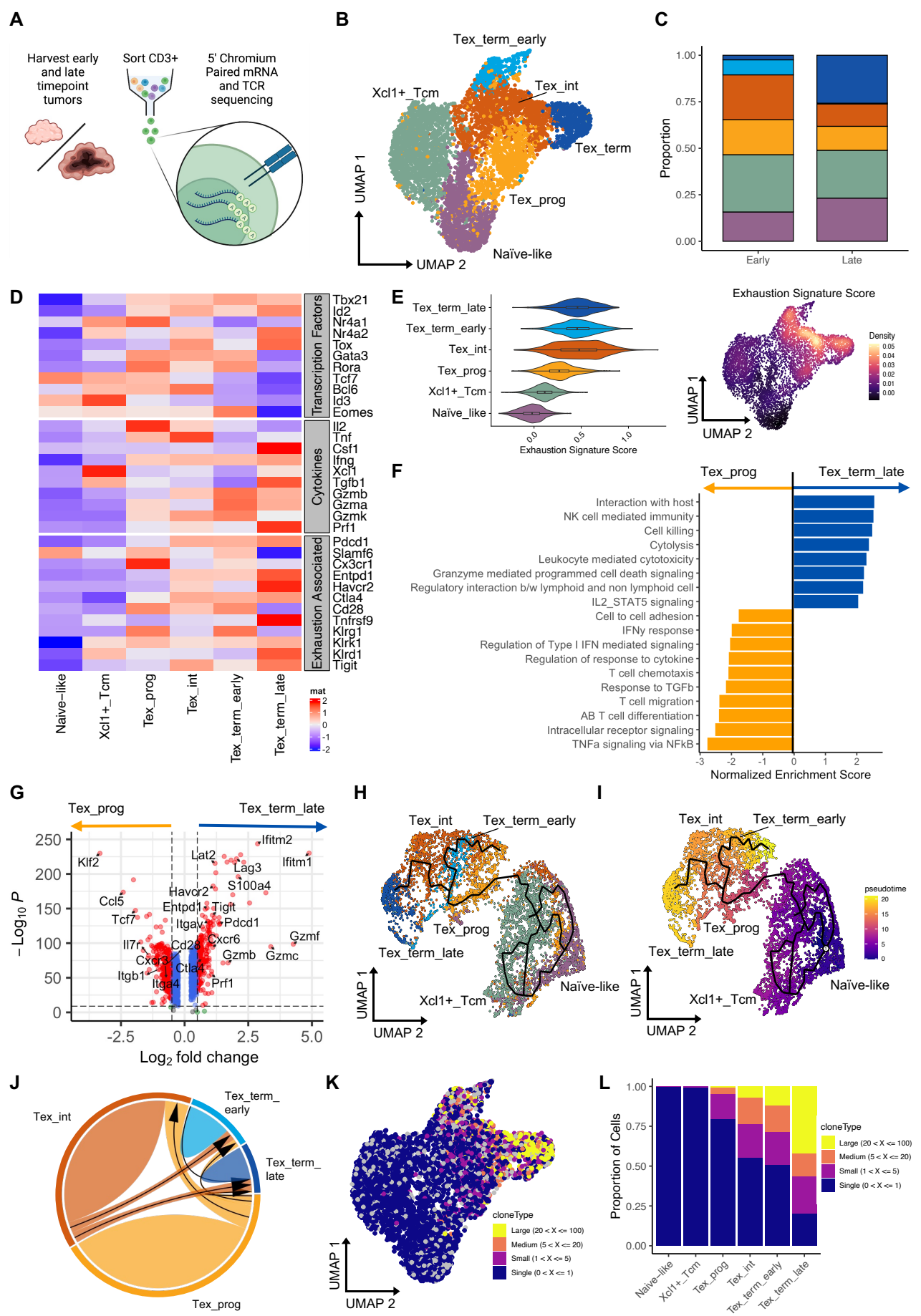


**Figure 2: scRNAseq defines transcriptional heterogeneity amongst tumor-infiltrating Tex_prog and Tex_term with an enrichment for cell-cell communication pathways in Tex_prog**

**Figure 2: scRNAseq defines transcriptional heterogeneity amongst tumor-infiltrating Tex_prog and Tex_term with an enrichment for cell-cell communication pathways in Tex_prog**

(A) Experimental layout for scRNAseq experiment. tumors were harvested at an early (D13) and late (D19) timepoint. Created with Biorender.
(B) UMAP of 6 CD8 T cell clusters following QC.
(C) Frequency of each cluster per timepoint.
(D) Heatmap of exhaustion associated transcription factors, cytokines/secreted molecules, and surface markers.
(E) AddModuleScore of exhaustion signature from Im et al., 2016, violin plot and density plot representations.
(F) Significantly upregulated pathways in Tex_prog and Tex_term from Hallmark, Reactome, Gene Ontology databases.
(G) Relevant genes from upregulated pathways in H.
(H) Trajectory analysis overlaid onto clusters from B.
(I) Trajectory analysis overlaid onto pseudotime.
(J) Circle plot of overlapping clones across Tex_clusters. Tex_prog, Tex_int have overlapping clones with all other clusters. Tex_term and Tex_int_2 do not have overlapping clones.
(K) UMAP of cloneTypes across clusters.
(L) Frequency of cloneTypes across clusters.
See also Figure S2.

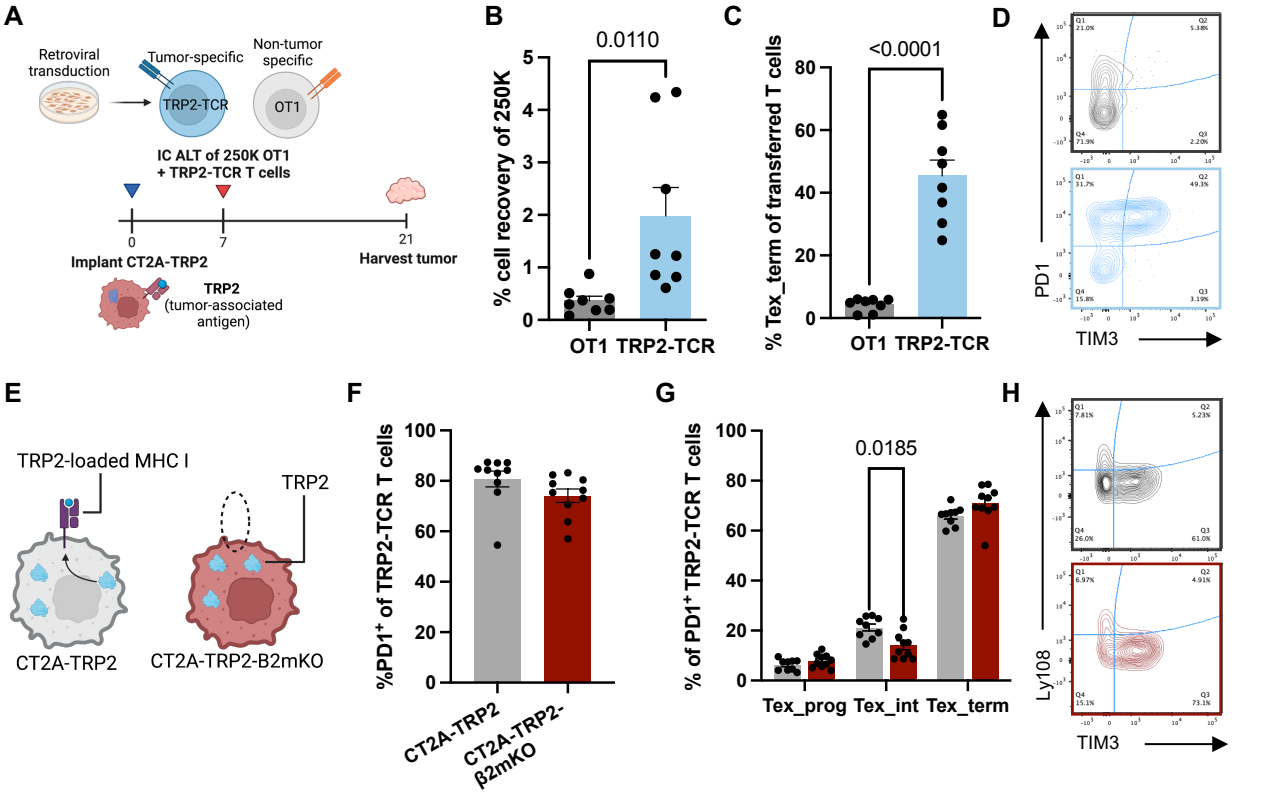


**Figure 3: Tumor cells are not a necessary source of the TCR stimulation mediating Tex_prog to Tex_term transition**
(A) Experimental layout. 250K *ex-vivo* activated and transduced OT1 and TRP2-TCR T cells were intracranially implanted into D7 CT2A-TRP2-bearing mice. Tumors were harvested 14 days later.
(B) Frequency of implanted cells recovered on D21. n = 7 mice/group.
(C and D) Frequency of PD1+ CD8+ T cells in OT1 vs. TRP2-TCR (C) and representative contour plot PD1 and TIM3 expression of OT1 and TRP2-TCR T cells 14 days post-transfer (D). n = 7 mice/group
(E) Experimental layout. 50K CT2A-TRP2 or CT2A-TRP2-B2mKO were implanted intracranially and harvested when mice were moribund. Created with Biorender.
(F) Frequency of PD1+ TRP2-TCR T cells between groups. n = 10 mice/group.
(G and H) Frequency of Tex subset of PD1+TRP2-Tetramer+ CD8+ T cells and representative contour plot (G) and representative contour plot of Ly108 and TIM3 expression between groups (H). n = 10 mice/group.
p-values are shown on individual plots as measured by two tailed t-test (B, C, F) or RM 2-way ANOVA (G). See also Figure S3.

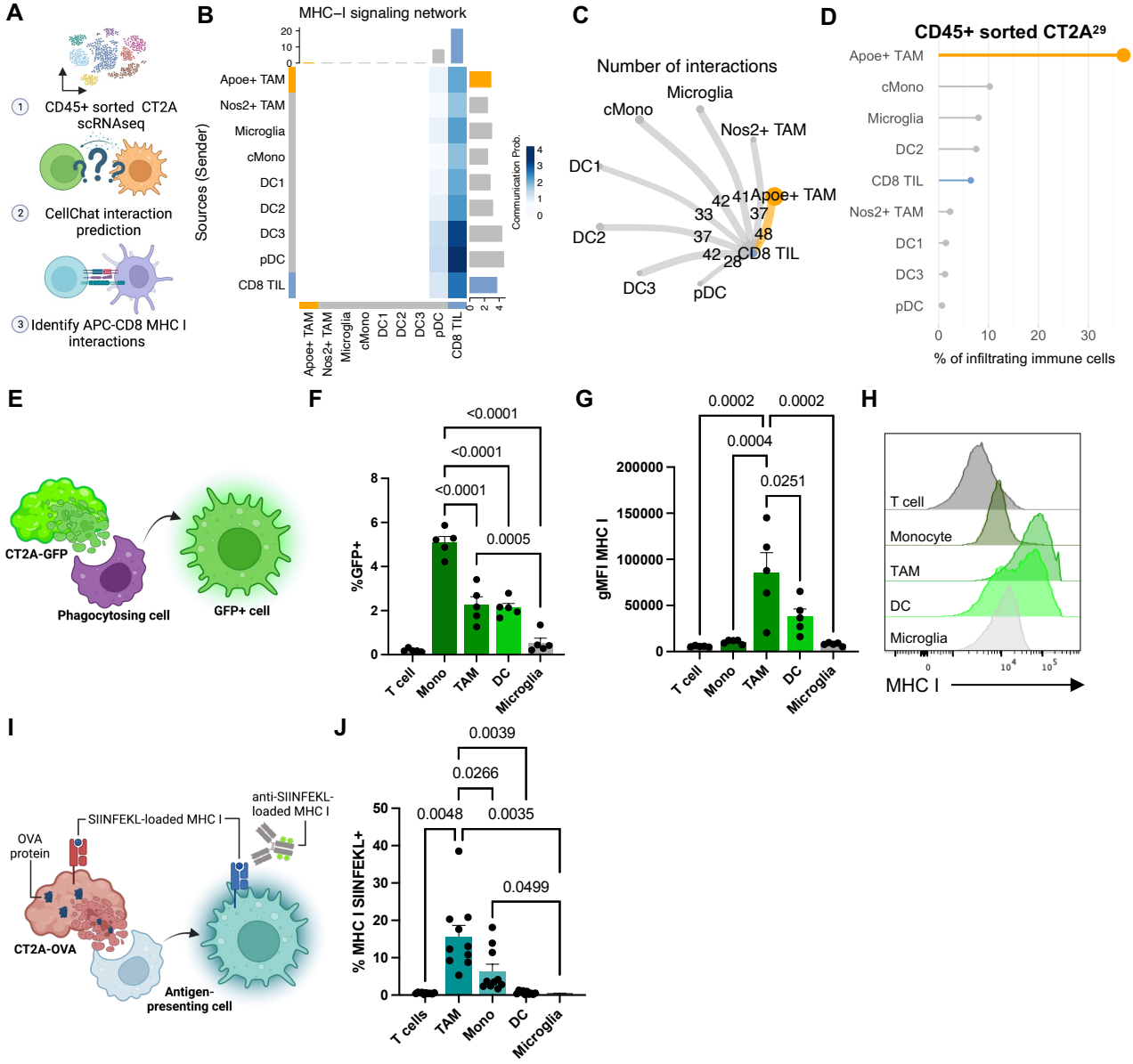


**Figure 4: TAM are the most frequent and most potent cross-presenting antigen-presenting cells (APC) within the intracranial TME.**

(A) Experimental layout. CD45+ sorted scRNAseq from Tomaszweski et al., 2022 was analyzed with CellChat to determine which APC had predicted MHC I interactions with CD8 T cells. Created with Biorender. ## = reference

(B) Heatmap showing communication probability of MHC I interactions in the TME. All APC were predicted to interact with CD8 TIL through MHC I.

(C) Circle plot displaying number of interactions (thickness of arrow/number) across APC populations.

(D) Frequency of infiltrating immune cells from Tomaszewski et al., 2022 dataset.

(E) Experimental layout. 25K CT2A-GFP was implanted intracranially and harvested when mice were moribund. GFP+ APC were evaluated. Created with Biorender.

(F) Frequency of GFP+ T cells ($CD3^+$), TAM ($CD45^{hi}CD11b^+F4/80^+$), DC ($CD11b^+MHC\ II^+F4/80^-$) and Microglia ($CD45^{hi}CD11b^+F4/80^+$). n = 5 mice.

(G and H) gMFI of MHC I of APC populations from F (G) and representative histogram (H). n = 5 mice.

(I) Experimental layout. 100K CT2A-OVA was implanted intracranially and harvested when mice were moribund.

(J) Frequency of SIINFEKL-loaded MHC I of T cells, TAM, Monoctyes ($CD11b+F480^{int}Ly6C^{hi}$), DC, and Microglia. n = 9 mice.

p-values are plotted on individual graphs. Statistical significance was determined by 1-way ANOVA (F, G, J) with post-hoc Tukey's test for multiple comparisons. All data are plotted as mean ± SEM. See also Figure S4.

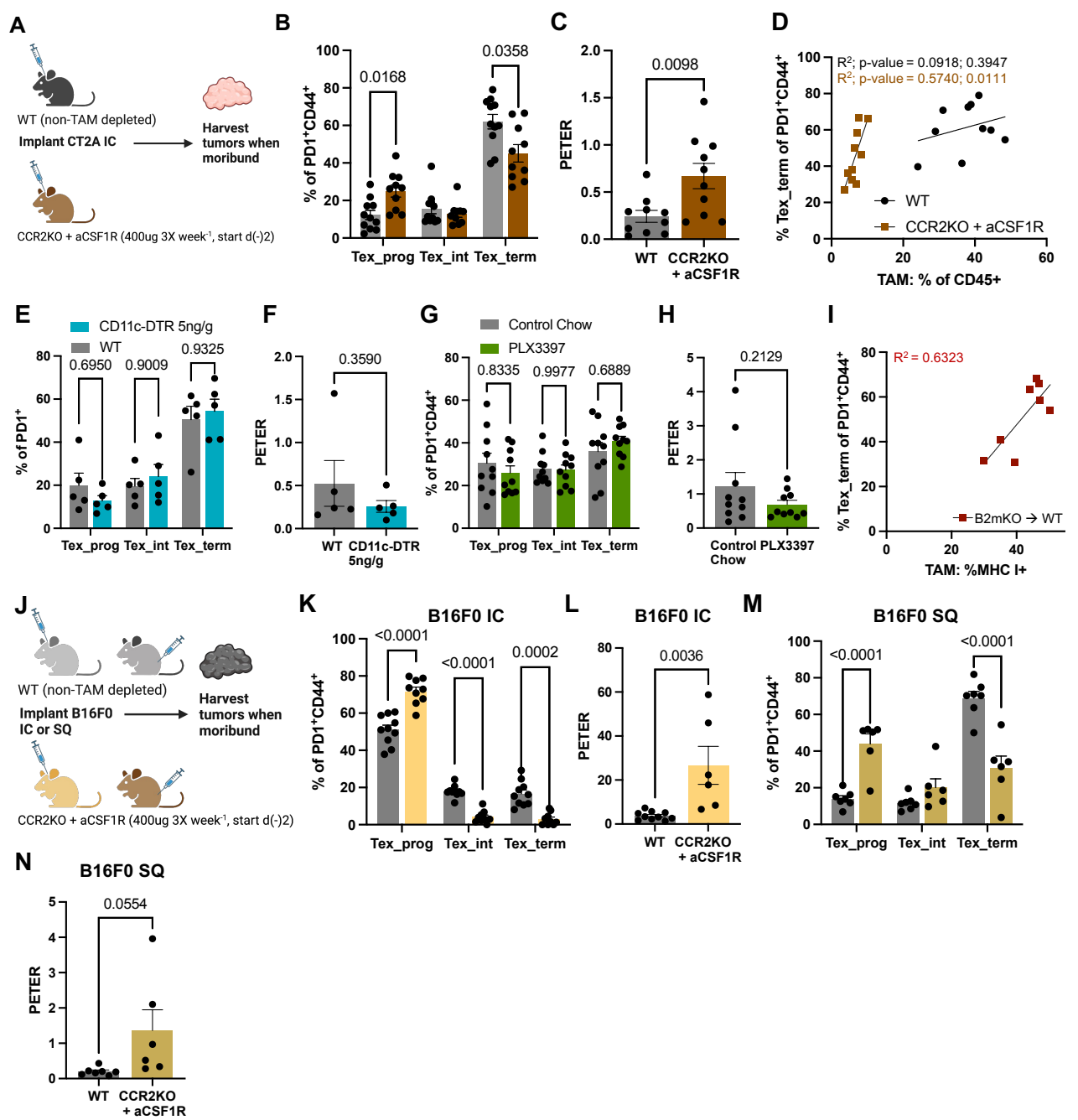


**Figure 5: TAM mediate progenitor to terminal exhaustion transition in GBM and other intracranial solid tumor models**

(A) Experimental layout. TAM and monocytes were depleted in CCR2KO mice with aCSF1R depletion antibody. 10K CT2A was implanted intracranially and harvested when mice were moribund. Created with Biorender.

(B and C) Frequency of Tex_subsets of PD1+CD44+ (B) and PETER between WT and TAM depleted groups (C). Data pooled from 2 independent experiments. n = 10-11 mice/group.

(D) Simple linear correlation of %Tex_term of PD1+CD44+ CD8+ T cells vs. % TAM of CD45+. Data pooled from 2 independent experiments. n = 11 mice/group.

(E and F) CD11c+ DC were depleted with 5ng/g DTR injections on D8, D11, D14, D17 post CT2A-implantation. Frequency of T cell exhaustion subsets (E) and and PETER between WT and DC depleted groups (F). n = 5 mice/group.

(G and H) Microglia were depleted with 290mg/kg PLX3397 free-fed chow starting 1 week prior to CT2A implantation. Frequency of T cell exhaustion subsets (G) and PETER between WT and microglia depleted groups (H). n = 10 mice/group.

(I) Simple linear correlation of frequency of Tex_term vs. Frequency of MHC I+ TAM in B2mKO chimera mice implanted with CT2A.

(J) Experimental layout. TAM and monocytes were depleted in CCR2KO mice with aCSF1R depletion antibody. 1K B16F0 was implanted intracranially or 100K B16F0 was implanted subcutaneously and harvested when mice were moribund. Created with Biorender.

(K and L) Frequency of Tex_subsets of PD1+CD44+ B16F0 IC (K) and PETER between WT and TAM depleted groups (L). n = 9-10 mice/group.

(M and N) Frequency of Tex_subsets of PD1+CD44+ B16F0 SQ (M) and PETER between WT and TAM depleted groups (N). Data pooled from 2 independent experiments. n = 6-7 mice/group.

p-values are plotted on individual graphs. Statistical significance was determined by two-sided unpaired t test (C, F, H, L, N) or RM-2-way ANOVA with post-hoc Tukey's test for multiple comparisons (B, E, G, K, M). All data are plotted as mean ± SEM. See also Figure S5.

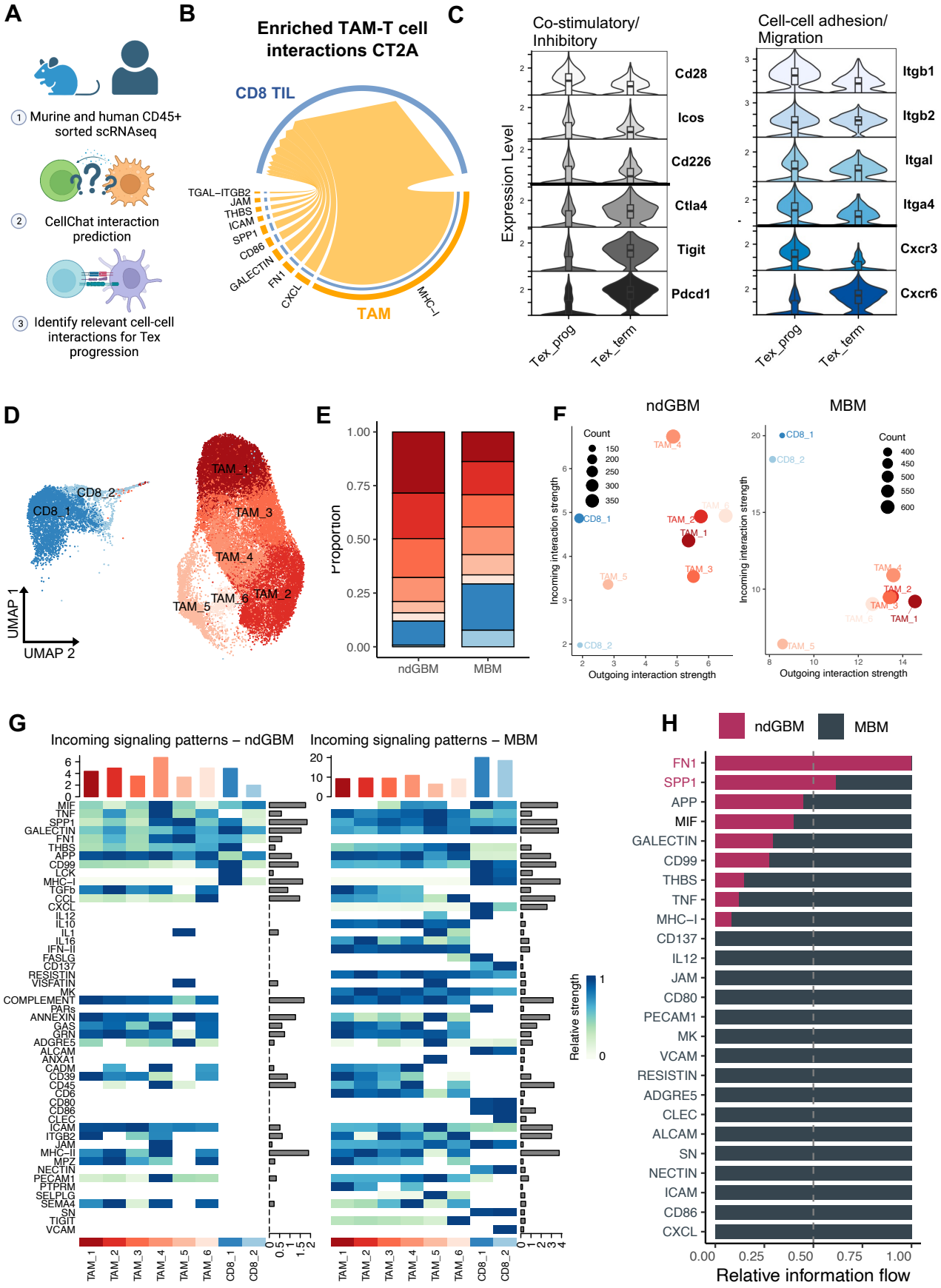


**Figure 6: CellChat predicts secondary interactions between TAM and CD8+ T cells in mice and humans that may contribute to exhaustion progression**

**Figure 6: CellChat predicts secondary interactions between TAM and CD8+ T cells in mice and humans that may contribute to exhaustion progression**

(A) Experimental layout. CD45+ sorted scRNAseq from murine GBM, ndGBM and MBC was analyzed with CellChat to determine additional TAM-T cell interactions. Created with Biorender.

(B) Enriched predicted interactions with TAM (orange) as the source and CD8 TIL (blue) as the target from murine GBM.

(C) Receptors expression in Tex_prog vs. Tex_term from CD3+ sorted dataset from Figure 2 of predicted interactions from 6B.

(D) UMAP of human ndGBM and MBM datasets.

(E) Frequency of TAM vs. CD8s in ndGBM vs. MBM.

(F) Incoming vs. outgoing interaction strength across cell types in ndGBM vs. MBM.

(G) Heatmap of all incoming signaling patterns in ndGBM vs. MBM.

(H) Significantly upregulated predicted pathways in ndGBM (maroon) vs. MBM (grey).

# Supplemental Figures

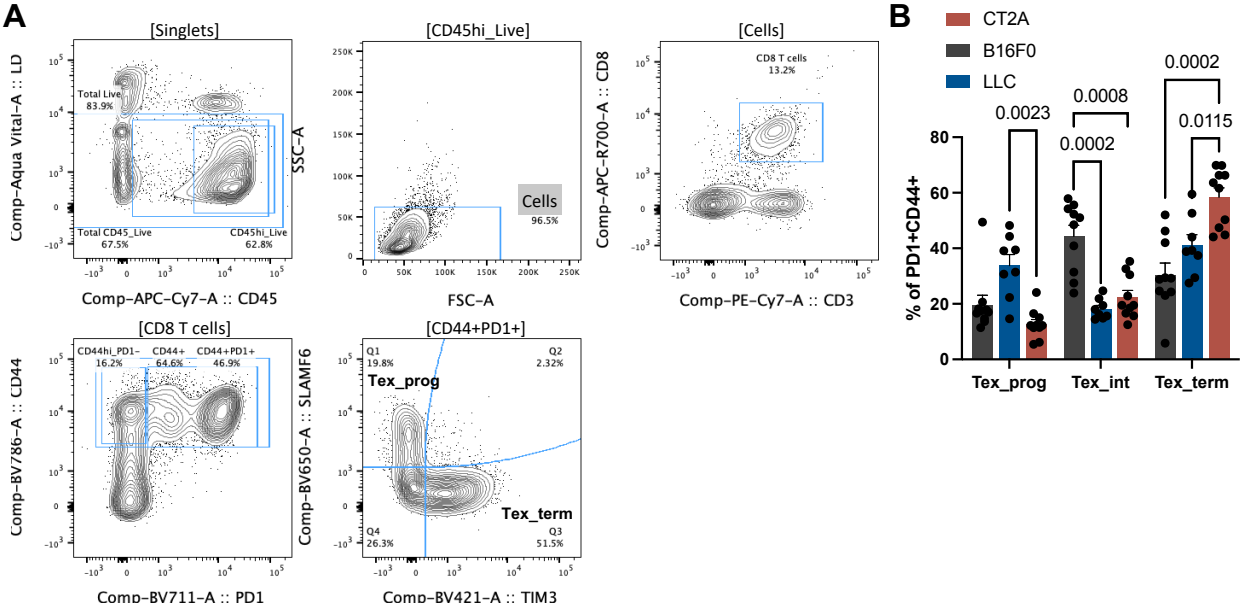


**Supplemental Figure 1:**
(A) Gating strategy for Tex_prog and Tex_term.
(B) Frequency of Tex subsets of PD1+CD44+ CD8+ T cells in intracranial B16F0, LLC or CT2A. n = 8-10 mice/group.
All of the data are means ± SEMs; p-values are shown on individual plots as determined by 1-way ANOVA and post-hoc Tukey test (B).

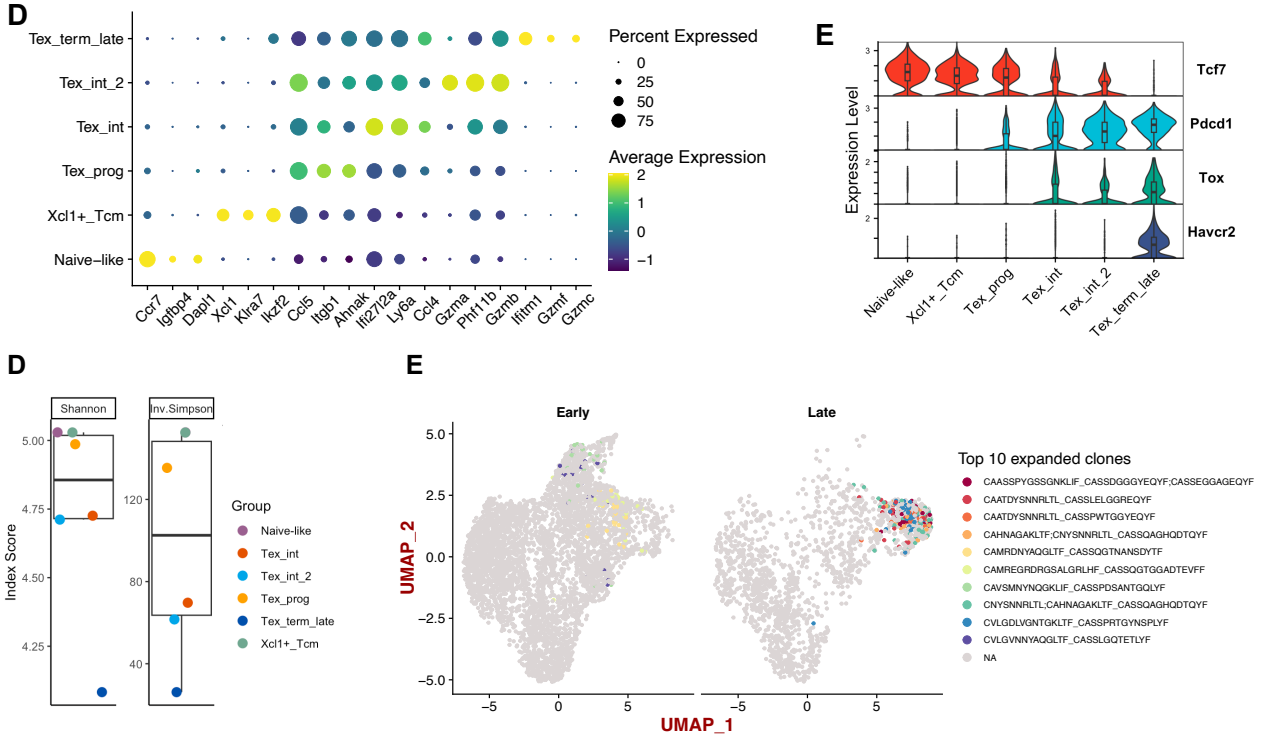


**Supplemental Figure 2**

(A) Dot plot of top 3 genes for each cluster.

(B) Violin plot of *Tcf7, Pdcd1, Tox,* and *Havcr2* expression across clusters.

(C) UMAP of cloneType across biological replicates (n=4 per timepoint).

(D) Shannon and Inverse Simpson diversity indices across clusters.

(E) 10 most expanded TCR clones across timepoints are concentrated to Tex_int and Tex_term clusters.

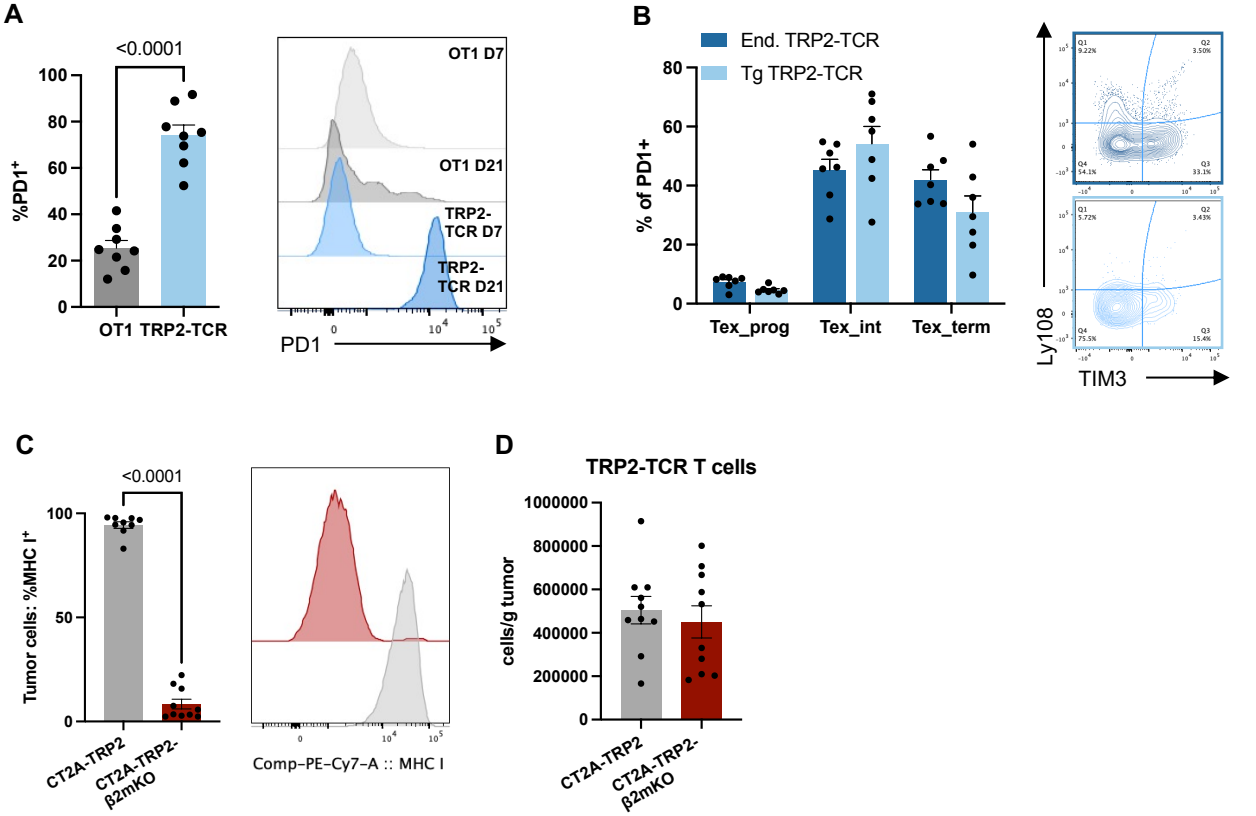


**Supplemental Figure 3:**
(A) PD1 expression on transferred OT1 vs. TRP2-TCR Tg T cells on day of ALT (D7) and day of tumor harvest (D21) and representative histogram. n = 7 mice/group.
(B) Frequency of Tex subsets of PD1+ endogenous or transgenic TRP2-TCR T cells and representative contour plot. n = 7 mice.
(C) gMFI of MHC I in CT2A-TRP2 vs. CT2A-TRP2-B2mKO validating knockdown of MHC I. n = 10 mice/group.
(D) Number of TRP2-TCR T cells/g of tumor in CT2A-TRP2 vs. CT2A-TRP2-B2mKO. n = 10 mice/group.
p-values are plotted on individual graphs. Statistical significance was determined by two-sided unpaired t-test (A, C, D) or 2-way RM ANOVA with post-hoc Tukey's test for multiple comparisons (B). All data are plotted as mean ± SEM.

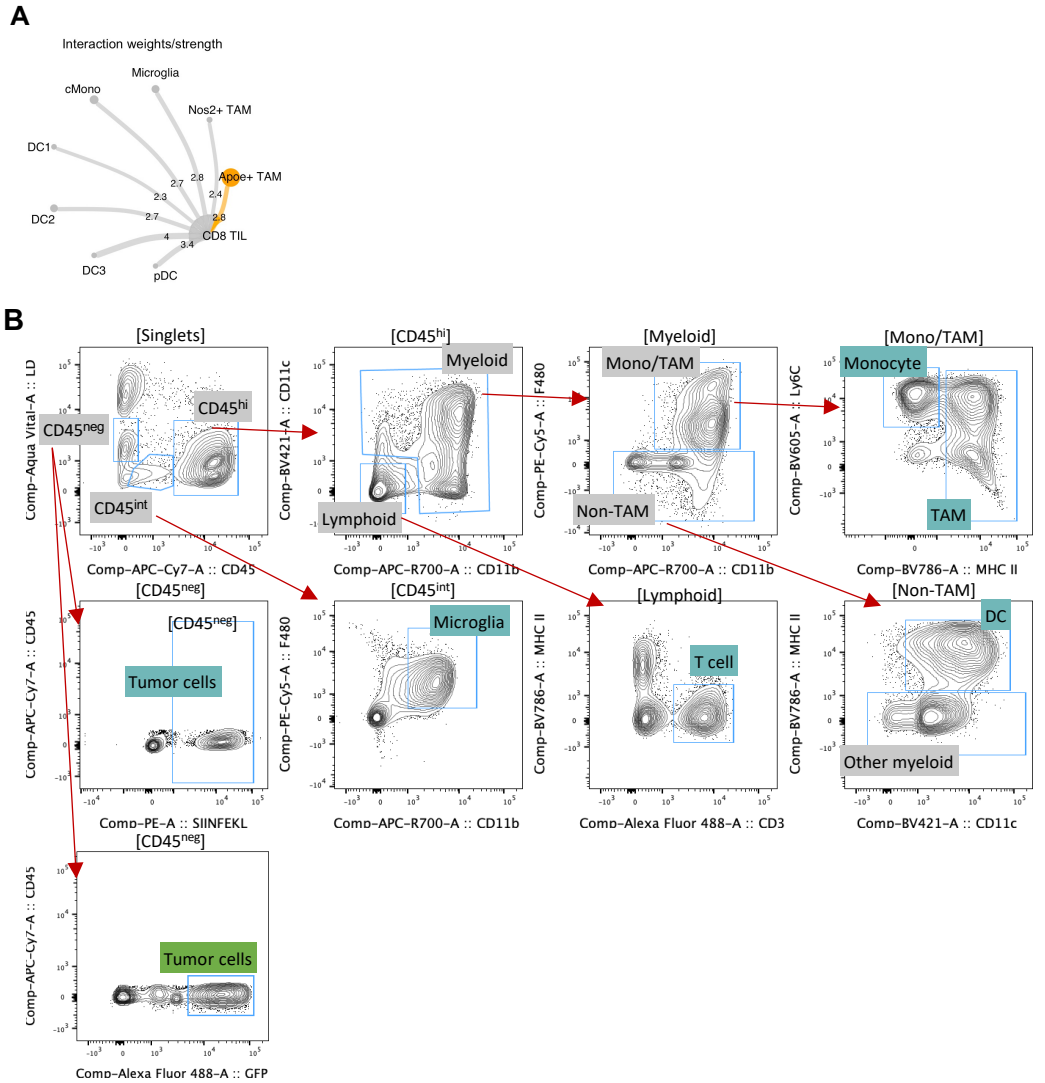


**Supplemental Figure 4:**
(A) Interaction strength across APC with CD8 TIL as the target.
(B) Gating strategy for intratumoral APC.

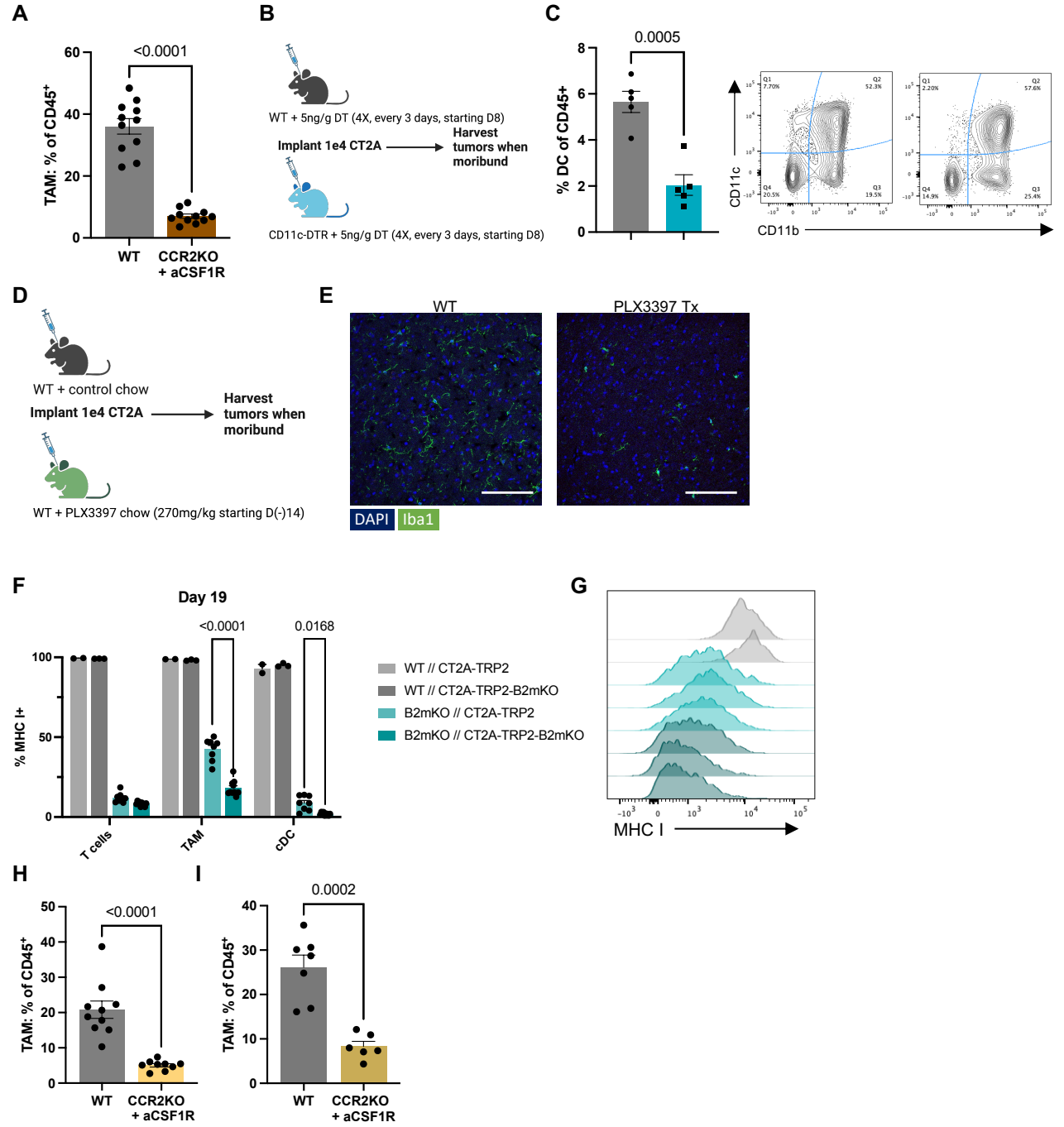


**Supplemental Figure 5:**

(A) Frequency of TAM of CD45+ cells. Data pooled from 2 independent experiments. n = 11 mice/group.

(B) Experimental layout. DC were depleted in CD11c-DTR mice with 5ng/g DT, every 3 days for 4 total treatments, starting D8. Created with Biorender.com.

(C) Frequency of CD11c+CD11b- DC in WT vs. CD11c-DTR mice.

(D) Experimental layout. Microglia were depleted in WT mice with 270mg/kg PLX3397 chow. Chow was provided starting D(-)14. Created with Biorender.com.

(E) Representative immunofluorescence image of WT vs. PLX3397 treated non-tumor brain. Scale bar = 100um.

(F) Chimera validation. Frequency of MHC I+ in WT → WT (WT) or B2mKO → WT (B2mKO) chimeras across T cells, TAM and cDC. n = 8-10 mice/group.

(G) Representative histogram of MHC I expression on TAM in the setting of CT2A-TRP2 (Teal) vs. CT2A-TRP2-B2mKO (Dark Teal).

(H) Frequency of TAM of CD45+ cells in B16F0 IC. n = 9-10 mice/group.

(I) Frequency of TAM of CD45+ cells in B16F0 SQ. Data pooled from 2 independent experiments. n = 6-7 mice/group.

p-values are plotted on individual graphs. Statistical significance was determined by two-sided unpaired t test (A, H, I) or RM-2-way ANOVA with post-hoc Tukey's test for multiple comparisons (F). All data are plotted as mean ± SEM.